Design, production and testing of RF resonators and spin active material

University of Strathclyde

NPL

MPhil

2022

Abubakr Qaasim

Signed: *Abubakr Qaasim*

Date: 11/12/2022

Table of Contents

1 Abstract

RF resonators with a resonance in the GHz range were designed, produced, and tested in a dilution refrigerator, along with the design and simulation of spin active material from 4H-SiC material. The resonators were designed to have a resonance frequency of 2GHz and 3GHz and obtained a frequency of 1.93GHz , 3.03GHz and 3.13GHz. Experimental results show that these resonances were produced. The resonators were optimised to couple with spins, and design features were put in place to reduce energy loss to the environment. The resonators and the spin active material are thought to create a pairing which in the future could lead to a quantum memory for superconducting qubits.

2 Introduction

Defects in 4H-SiC are obtaining increasing amounts of interest in the scientific community along with other defects such as the NV centres in diamond and other materials (Y. Kubo, 2010), due to the promising research being done into the sensing and spin capabilities of some of these defects. These capabilities are of interest due to the increasing number of sensors being used in modern devices and provides an avenue to enable advanced monitoring and usage of devices. The main usage of the of sensors are to sense the magnetic field. There are other quantities such as pressure, electric field and temperature which can be measured optically (S. A. Tarasenko, 2018). This opens a whole field of using the optical properties of defects in situations where perhaps having an electrical sensor may not be feasible.

Another avenue of interest is the usage of these defects as a memory storage for quantum computing in the future, and as a quantum memory if the interface between the spins and superconducting qubits becomes feasible to create and use (A. K. V. Keyser, 2020). The interface provides many challenges due to the difficulties in coupling the spins and superconducting qubits as there are many ways in which energy could be lost rather than coupling and crossing the interface. The isolation of the system to the environment is very important in most cases to ensure the quantum state is not lost.

Research was predominately done on the creation of these defects using theoretical and technical aids along with the design, creation and testing of the interfacing resonators which would couple to the spins. The theoretical aids included conformal mappings and other calculations (R. Igreja, 2004), which when combined with simulations provided a means of estimating the parameters which would be measured using experimentation, such as frequency and defect concentration. The method of theoretically estimating, simulating, and producing the resonators to a specified frequency worked very well and the frequency matched very well.

Initially, in chapter 3: Vacancies in 4H-SiC, the defects in 4H-SiC are introduced and some of the features of the defects are explained. This includes the types of defects that are present in SiC and the formalism behind the common naming conventions for these defects.

Chapter 4: Defect Creation Simulation and Optimisation to a magnetic field outlines how the implantation of the 4H-SiC was simulated and how the implantation could be optimised to the resonator design, including the theory.

The focus then moves onto the resonator in chapter 5:Resonator Design, which includes an introduction to different types of resonators and how the resonators used in the experiments were designed. Chapter 6: Resonator Production talks about the method that the resonator was produced.

The focus turns to the measurement of the resonators which were produced with chapter 7: Measurement design talking about the methods which were to be used in the measurement and also adds in further experiments which could be done which is based on quantum theory.

Chapter 8: Testing Equipment and method, talks about the equipment used for the tests, and begins by explaining the details behind how the dilution refrigerator functions. The experimental equipment is also explained to guide the reader.

Chapter 9: Testing of the resonators discusses the data analysis of the experiments and how the data is processed to obtain the parameters required. The results section is included in chapter 10: Results, with the results being given context in chapter 11: Discussion. The conclusion is presented in chapter 12: Conclusion with references presented in chapter 13: References.

The overall results show that a low impedance resonator can be produced and resonate at its designated frequency. The spin ensemble could also be tailored in a way which would optimise the spin coupling. The resonator system along with the spin ensemble would provide a means to introduce a quantum memory.

3 Vacancies in 4H-SiC

Silicon carbide has many different configurations. These are named using a certain convention and have different properties depending on the type of defect. Shown below in Figure 3.1 is one example of a defect in 4H-SiC and the corresponding energy levels are shown on the right. This chapter aims to look at the different configurations and explains in detail the nomenclature of the different ways in which the SiC structures are ordered.

3.1 Energy levels of V2 4H-SiC

The single silicon vacancy on the cubic site (V2) in 4H-SiC is of interest as it is a spin active system and can be used to sense temperature (S. A. Tarasenko, 2018). Other defects do exist and are suitable for various applications. The V2 defect is a spin 3/2 system and the degeneracy can be split by using a magnetic field aligned along the c axis which is orthogonal to the hexagonal SiC layers.

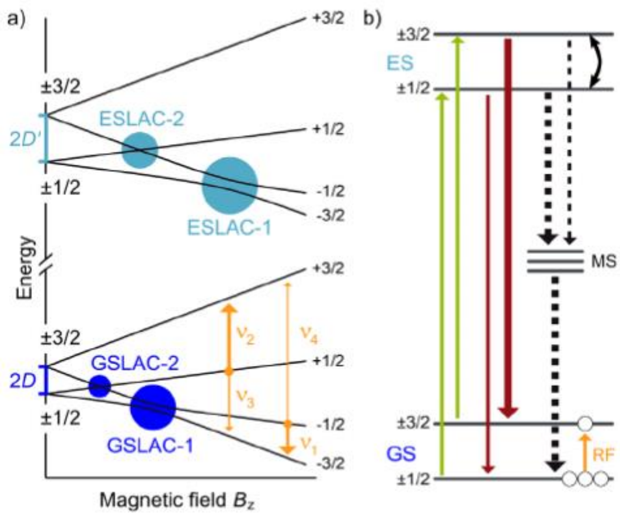

Figure 3.1: Picture showing the energy level diagram of V2 4H-SiC. On the left-hand side is a diagram showing how the different spin states change with different magnetic fields applied which results in a different energy spectrum. On the right-hand side, the metastable state is shown with the thicker line showing the most probable transitions. (S. A. Tarasenko, 2018).

The energy level diagram of Figure 3.1 shows that when the magnetic field increases, there is a change in the energy levels. The first change which occurs is a splitting of the spin states. This means that the +3/2 and -3/2 spin states which had the same energy level with no magnetic field present now have differing energy levels.

The second change is the change in the value of the energy levels as the magnetic field changes. This causes a change in the energy level differences at different magnetic fields which can be used to tune a defect into a resonance as the frequency of the incoming photon is related to the energy level difference.

This creates energy level anti-crossings when the m_z=-3/2 system crosses the m_z = ½ and m_z = -1/2 energy levels which occurs below 5mT when the magnetic field is aligned to the c-axis (S. A. Tarasenko, 2018),where m_z is the magnetic moment projection of the spin to the c-axis. The zero-level splitting, named as such as it describes the energy splitting of the 3/2 and ½ spins at zero magnetic field, 2D, is 70MHz for the ground state 3/2 and 1/2 states and is 401MHz for the excited level state 2D' (S. A. Tarasenko, 2018).

The right hand side of Figure 3.1 shows that the defect can be placed into a +3/2 spin state by optically shining a light to change the state of the defect to the excited state which is abbreviated to ES in the figure. This is due to the rate at which emission occurs and the +3/2 excited state going to the ground state is faster than the rate at which the +1/2 excited state goes to the ground state.

This example is the energy level of a defect in 4H-SiC. There are many different defects and corresponding energy level diagrams for the different defects. For this report, only a few are discussed. To better understand the defects a guide to the naming convention and formalism is important.

3.2 Polytypes of SiC

Silicon carbide has many different allotropes. Some of the allotropes being 3C, 4H and 6H, which refers to a cuboidal structure for 3C, and a hexagonal structure of the silicon carbide which is in turn made of silicon and carbon atoms.

Some of the differences arise from the changes in the structure and the arrangement of the SiC atoms. The SiC molecule is not stacked on top of one another but rather the arrangement of each layer is offset so each SiC molecule is at a different site .A cross section of a SiC structure can be seen in Figure 3.2 with the different sites of SiC being represented by different shapes.

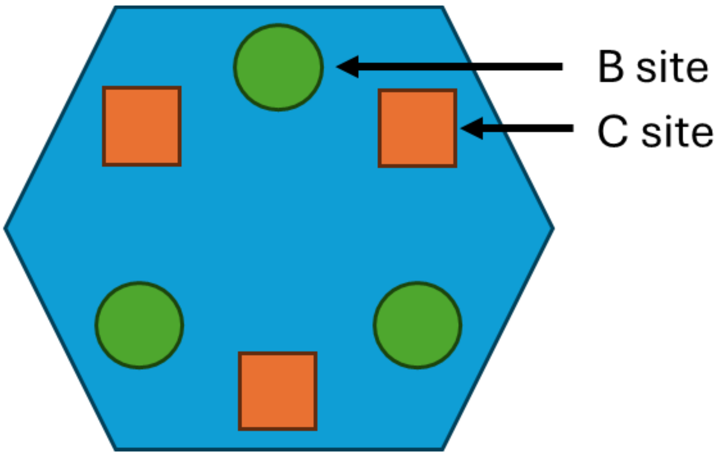

***Figure 3.2**: A hexagon with the circles showing the location of the B sites and the orange squares showing the location of the C sites. Typically, the structure has a hexagonal feature which is shown in blue. Different lattice structures consist of differing layers of the A, B and C site with the A sites consisting of an SiC molecule on the corners of the hexagon.*

The SiC lattice has many polytypes. This refers to the arrangement of each repeating block of single SiC bonds. The SiC structure is usually hexagonal which is usually denoted by a H. A number usually proceeds the H and this determines how many SiC bonds are stacked on top of each other before the pattern repeats.

For example, if one places a SiC molecule at each corner of a hexagon and one in the middle, a base can be created. If one proceeds to place another SiC molecule layer on top, there are two ways one could arrange the next layer without directly putting a SiC on top of each other in a uniform manner.

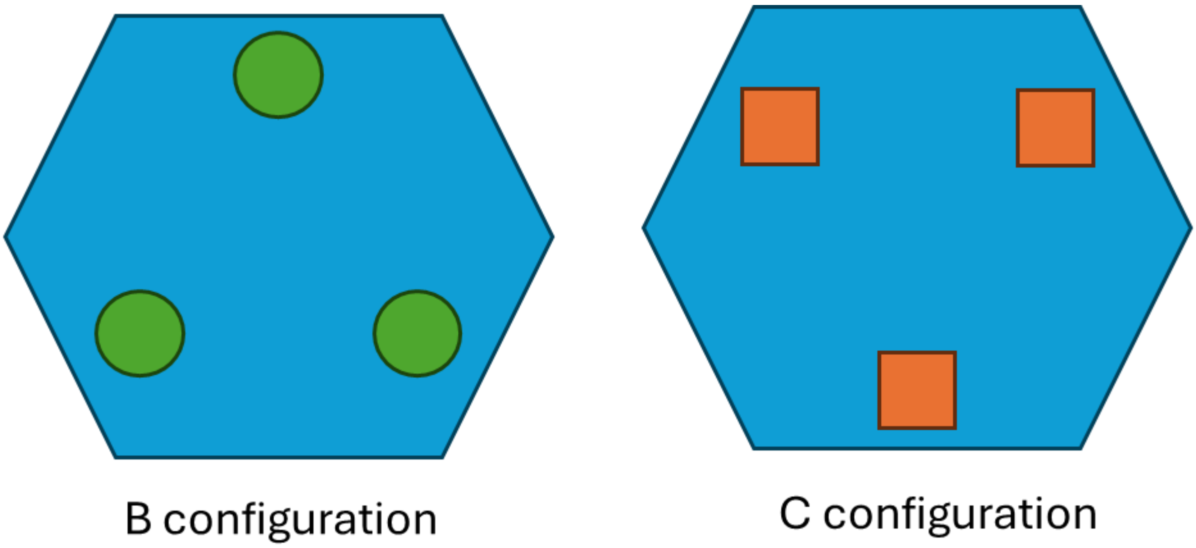

Figure 3.3: The equilateral triangle B configuration shown on the left and the inverted equilateral triangle C configuration shown on the right. The B and C configuration is the common manner in which to describe the structure of the lattice. The first layer is usually A with combinations of B and C after.

One way would be to place three molecules in an equilateral triangle shape in the hexagon, so each SiC molecule is halfway in between the midpoint of the hexagon and the edge as shown in Figure 3.3. Another way would be to place the three molecules in an inverted equilateral triangle, so the molecules again are halfway between the mid-point and the edge. If we call the base layer configuration A, the equilateral triangle configuration B and the inverted equilateral triangle C. The 4H lattice would be ABCB layers stacked on top of each other.

The 6H would be ABCACB and the 2H would be AB. The 3C would be ABC which can also be thought of as a cubic lattice thus the H is replaced with a C. In the remainder of this report we will be focussing on 4H-SiC.

3.3 Defects

Defects can be produced by creating damage in the silicon carbide which removes an atom in the lattice creating a vacancy defect. Replacing one of the atoms in the lattice with another atom creates an interstitial defect and many different defects can be created by various differing methods.

An example of this is a substitutional defect is where an atom is replaced with a different atom. Vanadium could replace a Silicon atom, and this would be known as a Vanadium substitutional defect.

The main defects in 4H-SiC are vacancies, with there being single vacancies and divacancies. The vacancy represents the absence of an atom and thus a defect in the material. A divacancy represents two adjacent atoms missing. The missing atoms creates a system which have their own energy levels.

Silicon vacancies in a 4H-SiC lattice are usually labelled as Vsi, but there is additional notation which related to whether this vacancy is located at the positions in the lattice with hexagonal lattice symmetry known as V1 sites and those with a cubic lattice symmetry known as V2 sites. The spectrum for the V2 sites can be seen in Figure 3.1 and will be the defect of most interest in our studies.

Care should be taken when indexing defects relating to 4H-SiC which relate to two atoms missing, displaced or replaced because if one atom defect is in a different layer this may create a different defect even though they seem similar, and the electronic configuration may be different, and this may lead to different energy level diagram.

So, to index these defects often an additional index is used. For example, when considering divacancies which pertain to two neighbouring vacancies, one being a silicon vacancy and the other being a carbon, one may think of the atoms on the A and C sites as h due to the fact that if you only included these molecular SiC layers they would look hexagonal.

Conversely, if one omits the A and C layers in 4H-SiC you would be left with the B sites and this would be a cubic lattice so these atoms can be indexed as k . So, in a divacancy, when the bottommost atom is taken from a hexagonal layer the index begins with a h and the topmost atom is taken from either the k or h layer giving the second index. Four combinations can be produced; (hh),(hk),(kh) and (kk). To avoid confusion between hk and kh, the bottom atom in each layer is denoted as being silicon. So hk would mean a carbon atom in h and a silicon atom in k.

The divacancy, a carbon vacancy next to a silicon vacancy, is of interest as its zero-field frequency is around the 1GHz mark which makes the resonator small enough to fit on a small-scale chip. The T2 time is said to be 1.25ms for the kk divacancy (D. Christle, 2015) and can vary according to the defect concentration. The divacancy also responds to electrical fields and thus stark shifts can be observed.

4 Defect Creation Simulation and Optimisation to a magnetic field

Defects can be produced in several ways, with differing quantities of different defects produced by each method. Some methods include laser induced damage (J. Liu, 2020) , Silicon and carbon implantation at differing energies and doses and proton (T. Ohshima, 2018) , electron (A. Kawasuso, 1997) or neutron irradiation (T. Suzuki, 1995).

For our simulations, carbon or silicon implantation was investigated as other elements would leave atoms which are not like the atoms already present in the material. The simulations started with mapping out where the vacancies would be created using the SRIM simulation software, the result of one simulation being shown in Figure 4.2. This was then turned into a probability as shown in Figure 4.1 to determine which implantation at which dose may be best for a specific resonator.

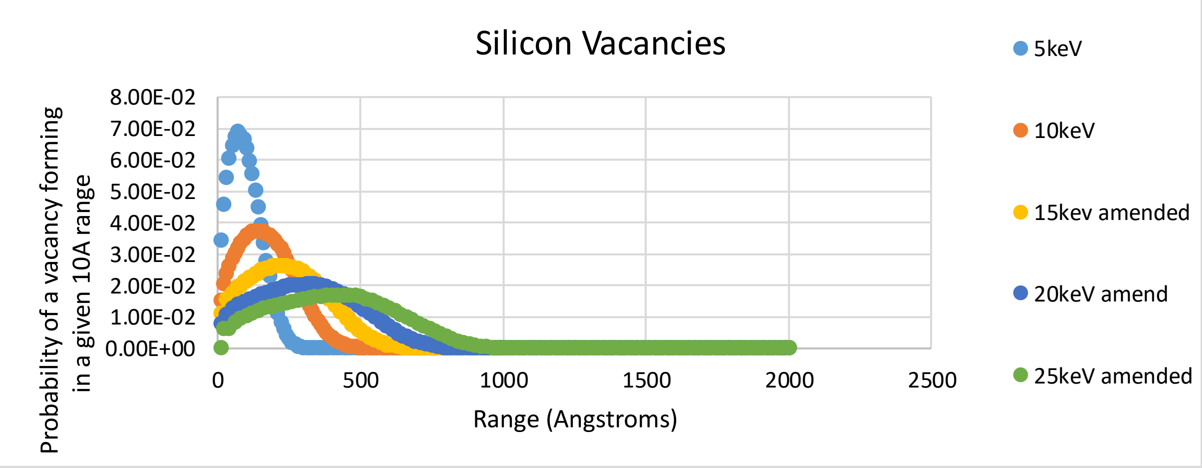

Figure 4.1:A graph showing the probabilities of a single Silicon vacancy being put at a certain 10A range. The different colours represent the different energies which the simulations were performed at. The graph shows that at higher energies, the vacancies are created further from the surface of the material and are more spread out and at lower energies the vacancies are created closer together and closer to the surface.

4.1 Defect Creation

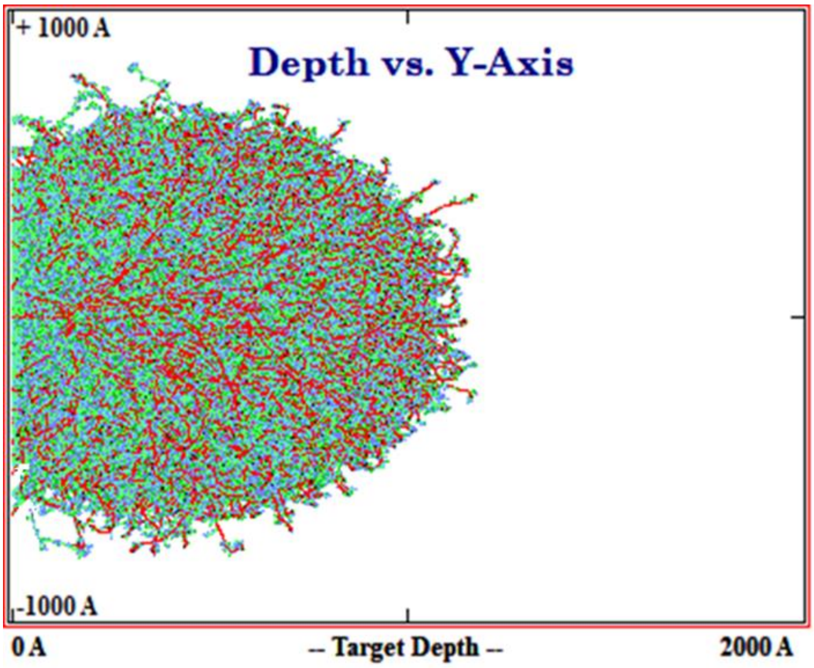

Figure 4.2: A graph showing a Monte Carlo simulation of a 25keV carbon ion into SiC performed using SRIM. The simulation shows that they are all created within 2000A of the surface of the material.

Initially, the defect creation needed to be optimised for the Si vacancy in SiC, so an appropriate choice would be carbon or silicon as the implantation species. Carbon was chosen and simulations in SRIM showed that the ion after entering the SiC would displace many carbon and silicon atoms, creating vacancies within the lattice as shown in Figure 4.2, which could then end up in a lattice site substituting for another atom in the lattice or become an interstitial defect where the ion is between lattice sites.

The vacancy creation can be optimised by simulating ions of differing energies with higher energies creating higher vacancies per ion. Simulations in SRIM were done to look at the effects of the incoming energy of the ion to the defect location and the defect amount per ion. The trend seemed to be that for higher implantation energies, more defects were created per ion and the defect concentration seemed to be less peaked with the peak being deeper into the material.

Different ions caused differing profiles of defect generation. In the future, the different ions with different energies could be used to make different defects for various applications. If the dose is low enough, one defect per implantation could be produced for a specific site which could be useful in the production of single photon emitters from one vacancy site.

Defects can react to electrical and magnetic fields in various ways. One of the ways in which the defects interact with fields is through the Zeeman effect which is an energy level splitting or change caused by the presence of a magnetic field. This causes the defect energy levels to change which in turn causes the spectra of the defect to change. Different defects react differently to different fields and studying these effects is one of the areas of research which provides valuable insight into which defect may be used for any application in the future.

4.2 Defect Creation Optimisation

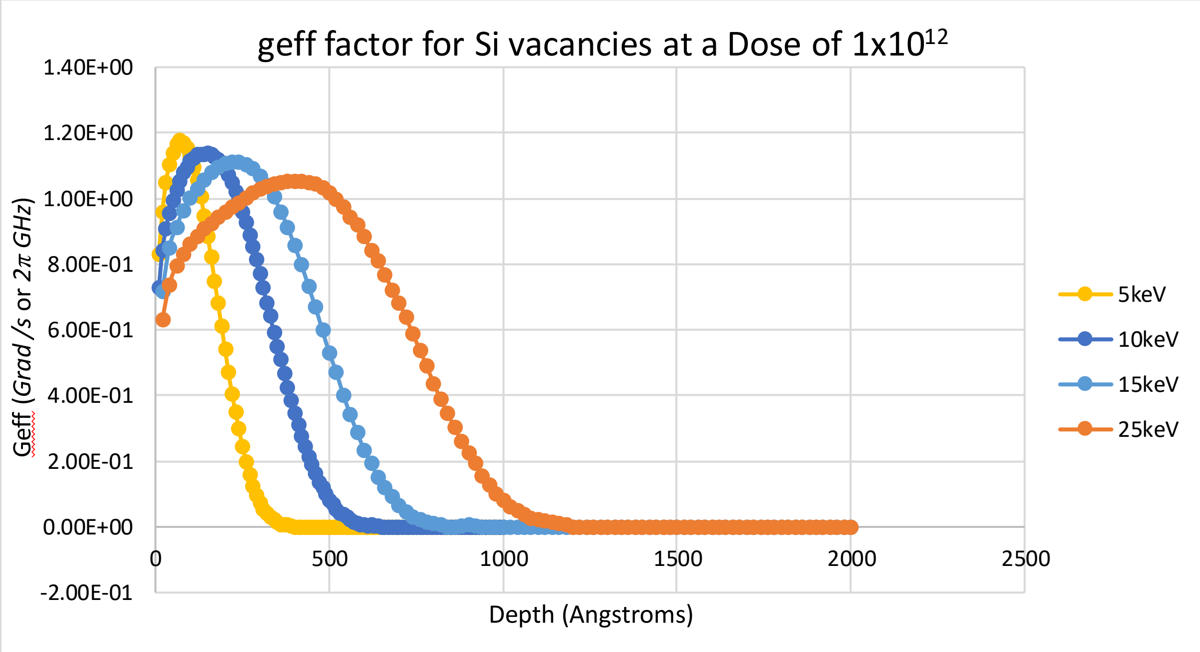

Figure 4.3: A graph showing the Silicon Defect coupling factor geff for different implantation energies and a dose of 1e12. The geff does not change much for the different energies although the depth of the defect has an effect.

Given the energy difference between two zeeman split spins is $g_s \mu_0 B \Delta S$ where g_s is the spin gyromagnetic ratio, and ΔS is the spin difference, the split can be equated to the coupling between the magnetic field and the atom which can be thought of as the coupling between the resonator and atom if the magnetic field is confined to a cavity. This would then give $hg = g_s \mu_0 B \Delta S$ where h is plancks constant and g is the coupling factor in hertz.

As the coupling factor would be very small this presents a problem, namely that the system must be measured before losses occur, and that the coupling would not be fast enough to occur before this happens.

One way to reach strong and fast enough coupling is by coupling loads of spin active defects to this magnetic field which gives an enhancement of $\sqrt{N}$ to the g factor where N is the number of spin active defects. The g factor could be different for different depths as the concentration of the ions may decrease or increase further down in the material, and thus the g factor would increase or decrease. The energy of the incoming implantation ion plays a part in this effect and Figure 4.3 shows the theoretical g profiles for the different energies to a specific resonator magnetic field.

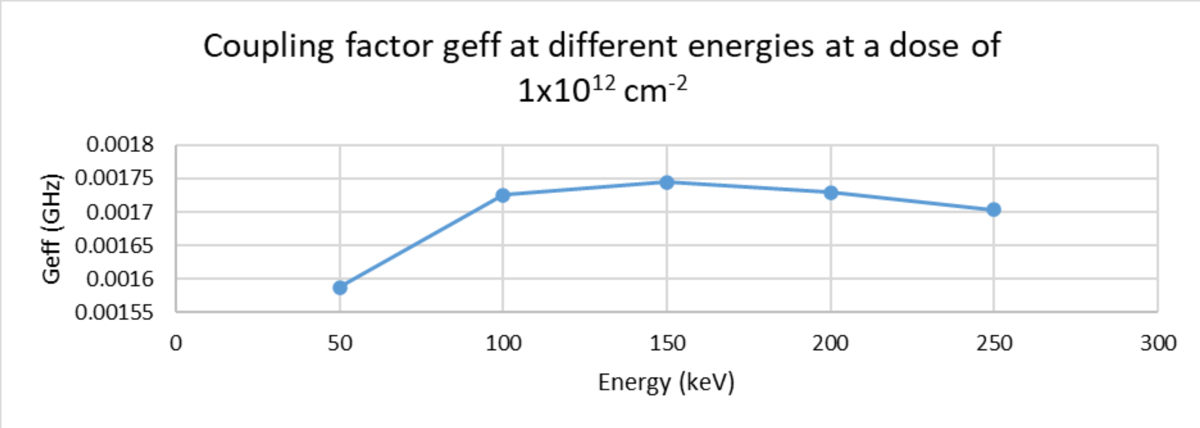

Figure 4.4: A graph showing the coupling rate geff at different energies at a dose of 1e12. The optimum implantation energy looks to be 150keV with a large drop-off of geff below 100keV. Energies above 150keV still have a large geff.

One problem with the concentration of defects not being uniform at all depths is that all the ions may not be experiencing the same magnetic field and hence the same coupling factor g, because they may be at different depths in the material or further away from the wire, and so this approximation of all the defects having the same magnetic field would be wrong.

One way to overcome this would be to take the root mean square of the magnetic field weighted by the number of defects at each depth. The number of defects could be approximated using the SRIM data which gives the number of defects within a certain depth range.

This can be converted into a density of defects for a given depth ρ and multiplied by the dose D, area A, and depth range dr to give N. If this is then integrated over all the defect for a given implantation energy with the magnetic field at a certain depth being calculated and squared. Analytically, the equation for gn can be given as:

$$g_n = \frac{2\pi S \mu_B g_s}{h} \sqrt{\int_0^R \rho'(r) {B_x}^2 A dr} \;\; (where\ \rho'(r) = D\rho\ and\ D\ is\ the\ dose)$$

Equation 4.1: Equation for gn.

In Figure 4.3 and Figure 4.4, different overall geff is calculated by approximating the magnetic field of a resonator at a point, and the spin density and integrating over the whole depth of the implantation. In this manner, the geff can be calculated for a specific implantation dose and a certain energy.

The implantation energy is changed in the graph above to find the optimum energy to obtain the best geff for a specific dose. Although one would think that the higher the energy the higher the number of defects created and thus the more likely the geff would be higher, the theoretical simulations show that this may not be the case.

This could be because at higher implantation energies, the peak of the vacancies created would be further away from the surface and would have a lower magnetic field being present which would lower geff. 150keV was found to be a crude estimate of the most optimum dose for the inductor and current through the wire with the magnetic field profile which was previously simulated.

4.3 Anneals

Defects in a material can be changed by annealing the defects. The defect's properties seem to be permanently changed and may be due to some of the damage near the defect being healed. At higher temperatures some of the smaller defects migrate and the defects can merge to become another defect. Temperature control of the annealing can affect the type of defect that is present in the final defect.

Heating the implanted SiC to 600C for roughly four hours has been shown to increase the fluorescence of defects (J. F. Wang). This may be evidence that more silicon vacancies are created by a post implant anneal and if it can be shown that the anneal increases the g factor this can indeed be told to be the case.

Increasing the temperature can create divacancies, with the optimum thought to be around 1400C. The process for making divacancies is thought to include the migration of silicon vacancies above a temperature of 700C into carbon vacancy sites.

This is further assisted by the movement of carbon vacancies at roughly above 1100C. Another reaction which involves a carbon vacancy moving into a carbon antisite defect is thought to be activated at 1100C. At roughly 1600C the divacancy is thought to be degraded and destroyed (N. T. Son, 2006).

4.4 Losses and coupling rate

Losses of the spin state to the environment and the photons in the resonator to the environment are a major problem when a coherent state is required as the state could be lost before any measurements or operations are performed on the system.

To mitigate this phenomenon, the coupling rate should be faster than the loss rates of the spin state which is usually assumed to be γ =1/T2 and the loss rate of the cavity κ which is normally given by the angular frequency of the resonator divided by the quality factor.

The cooperativity C is usually given as a measure of how well a particular coupled system performs with more than one being considered a good value to say that the system performs well and does not lose its state to loss before coupling and its equation is given by:

$$C = \frac{{g_{eff}}^2}{\kappa\gamma}$$

Equation 4.2: Equation for C.

Some spin systems have been shown to have a high cooperativity (D. I. Schuster, 2010), which is usually done by increasing g, but κ can also be decreased by decreasing losses in the resonator and γ can be decreased by ensuring the environment is as stable as possible but this is harder to decrease as there is intrinsic loss to the environment.

5 Resonator Design

The resonator design began with a review of the current resonators and looked at what the benefits of each different type of resonator presented. Some of the resonators reviewed are shown below in Figure 5.1 with an explanation of the way in which each resonator works.

The work then progressed to creating a new design, which starts with the feedline which represents the transmission line which couples to the resonator. Once the feedline was designed using the aid of calculations and simulations work on the resonator design began. The initial designs saw a low impedance resonator with the resonator in the middle and is discussed later on in the chapter. The calculations and evolution of the design is also mentioned.

One of the most important points about the resonator design is the inductor, and particularly the magnetic field from the inductor. For this reason, the magnetic field which is derived from the current flow was modelled and some of the simulations are shown later on in the chapter. The next chapter draws from the magnetic field profile of the resonator to optimise the implantation and produces a theoretical model.

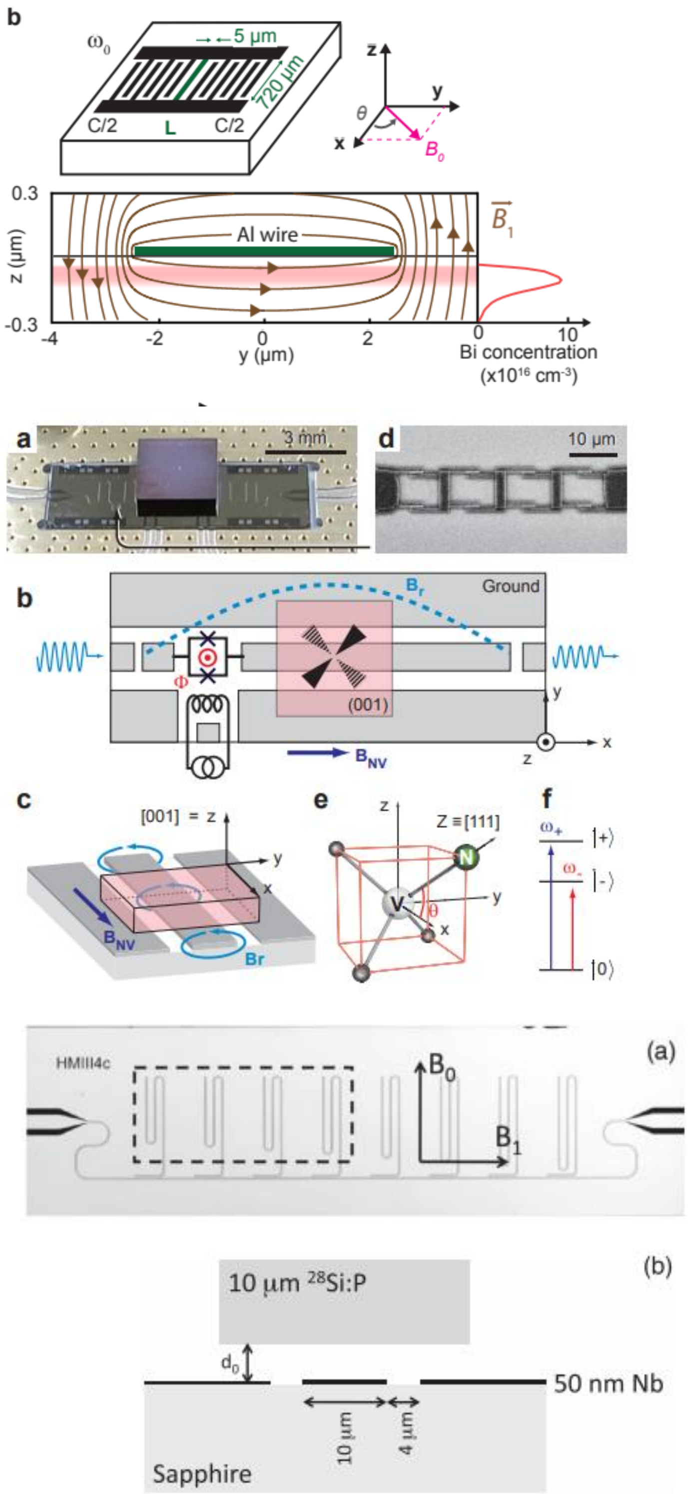

Figure 5.1:The design of different types of resonators from several different researchers (A.Bienfait, 2016), (Y. Kubo, 2010), (H. Malissa, 2013) . The top of the figure shows a half wavelength resonator. The magnetic field can be shown emanating above and below the waveguide which would couple with spins. The middle showing a half wavelength resonator with a

tuneable Josephson junction. A spin active material can be shown above the resonator which would resonate at the same frequency as the resonator with the josephson junction assisting in reaching this resonance. The bottom showing quarter wavelength resonators coupled to a coplanar waveguide. Various resonators are shown with varying lengths which translate to different resonances to allow spin active materials with varying resonances to couple to the resonator.

There are a plethora of superconducting microwave resonators designs to suit ones needs for a certain measurement (A.Bienfait, 2016), (Y. Kubo, 2010), (H. Malissa, 2013) . In Figure 5.1, the first resonator on the top is a simple lumped element resonator which has an interdigitated capacitor along with a wire in the middle which usually couples to the spins and is known as the coupling inductor. The capacitor and inductor make up a resonant circuit which then interacts with spin active material if the resonant frequency of the spins is similar to the resonance of the resonator.

Moving to the middle image, the resonator design is a half wavelength waveguide resonator. The resonator has its primary wavelength resonance at double the length of the resonator and has a squid element on one side of the resonator to make the resonant frequency tuneable. The spin active material is usually placed right on top of the resonator to allow the spin active material to resonate with the resonator.

The bottom picture in Figure 5.1 above shows several quarter wavelength coplanar waveguide resonators which allow the resonators to have differing frequencies so that the material which is usually placed above can be probed at several different frequencies. This method uses a coplanar waveguide as an input for the radio waves and the waves then go into the resonators with a certain coupling factor. This can be modelled, and the resonator can be thought of as coupling to the central coplanar waveguide (CPW) by a gap which can be modelled as a coupling capacitor, although mutual inductance could also play a part.

A lot of the work with coupling spins to resonators can be thought to arise from the need of the spin-resonator system to be strongly coupled and improving current systems to enhance this coupling. This is usually quantified with a coupling rate and compared against the coupling rate to the environment.

If the coupling rate to the environment is higher than the coupling rate of the spins to the resonator, the coupling is in the weak regime. To ensure that the coupling is strong, the coplanar waveguide resonators need to be well designed, and the design is strongly influenced by the modelling of the waveguide. Extra features to reduce such coupling to the environment were included and could be improved to reduce the loss rate.

Coplanar waveguide resonators can be modelled as an inductive and a capacitive element in series. Although the resonators have essentially the same elements there are some subtle differences. Some research has been done into which resonators may be suitable for certain applications.

For example, a low impedance resonator can be used as qubits if a Josephson junction is added. As the impedance would be low, this would mean that many of these low impedance qubits could be used with the addition of electrical fields to tune the resonators if required. Single radio frequency photons could also be detected using these resonators.

The high concentrated magnetic field would also mean that the resonator could be coupled to a spin system or a spin ensemble. This would allow energy to flow to and from a resonator to a spin ensemble, which in turn could allow higher memory retention times for quantum systems which use superconducting qubits.

There is also the possibility of using these resonators in systems which require amplification without noise being added to the system. This is particularly useful in cryogenic systems where parametric amplifiers could be used to initially amplify a signal from a device under test (DUT).

For spin coupling, quarter wavelength resonators have predominantly been used to couple with spins. Although quarter wavelength resonators can be useful for coupling to spins, lumped element resonators can also be used for coupling to spins and may provide an advantage. The lumped element resonators are usually high impedance which means that there is a low capacitive element or low impedance which means there is a high capacitive element.

In addition to the impedance of the resonator, which was modelled using the 2D design shown below in Figure 5.2, an impedance is present between the feedline CPW and the resonator and the strength of this coupling can be tuned by moving the resonator away from the feedline or towards it and can have an impact on the experiments, and ultimately how sensitive your measurements are.

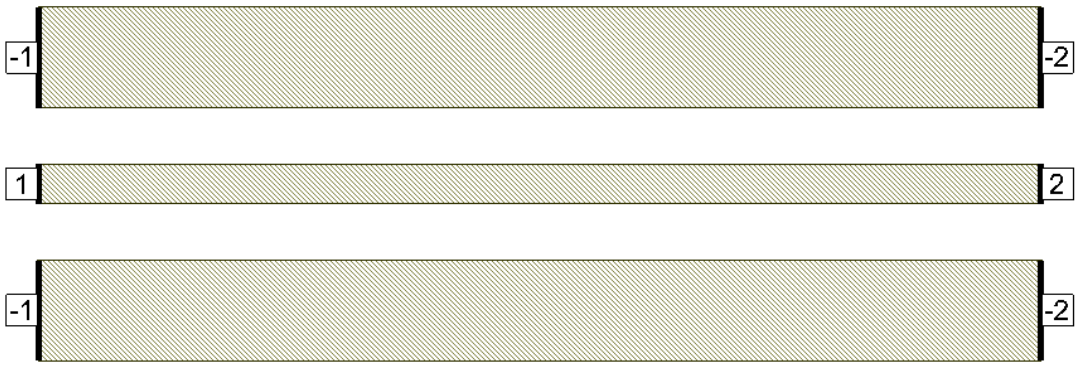

Figure 5.2: The design of the feedline used to test whether the feedline is matched to 50Ω. The centre line is the signal line, and the top and bottom shaded lines are the return lines. The shaded areas represent metallised areas with the non-shaded area having no material. The one and two are the signal and return ports with minus one and minus two being the ground return ports. The spacing of the feedline to the ground plane and the width of the feedline are crucial aspects in ensuring the feedline is matched to 50Ω.

5.1 Feedline considerations

When considering the feedline which will carry the microwaves, the main consideration is that the feedline should be impedance matched so there is minimal loss of signal when the wave enters and exits the feedline.

This is achieved in the design process by considering the dielectric constants of the material above and below the feedline and the spacing from the feedline to the ground plane. The equations governing the impedance and the capacitance of the feedline and hence the impedance can be solved, and the results can be obtained using conformal mappings (K. Watanabe, 1994), (M. Göppl, 2008).

For the base design a 50Ω line was chosen as this is an industry standard and a 5um feedline with 7um spacings to the feedline provided a 50Ω impedance matched feedline for SiC below the feedline and sapphire below the feedline.

Other feedlines can be designed with a 50Ω impedance. The way in which the feedline is modelled is by thinking of the feedline as capacitors in parallel and calculating the capacitance per unit length along with the inductance per unit length.

The capacitance can be thought to arise from the electric field between the central feedline and the ground plane, which is separated on either side of the feedline by a small gap. The feedline capacitance can be thought of as two capacitances, one capacitance coming from the electric fields connecting the feedline to the upper ground plane and the other capacitance coming from the electric fields connecting the feedline to the lower ground plane.

The capacitor geometries are then conformally mapped to a parallel plate capacitor geometry. The mapping involves taking a 2D capacitor and changing and mapping the geometry to make the capacitor into a standard parallel plate capacitor. The standard equation for the capacitance of the parallel plate capacitor is then used to obtain the capacitance. The inductance is found by relating the speed of the radio wave to the material parameters which are the permittivity and permeability of the material. Once the speed of the wave is known, the inductance is calculated, and hence the inductance equation which relates the capacitance and the speed of the wave to the inductance can be used to calculate the inductance. The inductance and capacitance are then used to calculate the impedance.

One of the other features which was added to the feedline was the tapering of the feeding. The feedline was tapered off towards the bond pads to maintain the integrity of the impedance and ensure there was not a sudden change in impedance.

The ends of the feedline were also strongly coupled to the ground plane by reducing the gap between the ends of the feedline and the ground plane. This was to ensure that the signal going from the bond pad to the end of the feedline was likely to be grounded rather than being reflected and affecting the signal coming from the feedline.

5.2 Low Impedance Resonator Design

The preferred choice for the resonator was a low impedance resonator which requires a high capacitance and a low inductance. Some simulations were done with a quarter wavelength resonator, the design and results of one design being shown in Figure 5.3. The low impedance design was chosen after considering the energetics of a resonator and how the energy flows from one form to the other.

In one cycle, a given excitation of energy would be stored as electrical energy in the capacitor and then as magnetic energy in the inductor. If the capacitance is high, the electric field will not be very high. This ensures the resonator will not interact with the surroundings as much and not create disturbance to the defects surrounding the resonator. This is crucial to mitigate any unwanted stark effects or other electrical coupling which may create loss.

The low inductance also assists in obtaining a high current and thus a strong magnetic field. This physically manifests itself as a very large capacitor with a very small inductor which can be thought of as a small constriction where preferably the defects will be, as this is where the current will be the largest and thus the magnetic field will be the strongest.

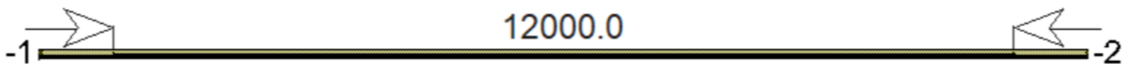

(a)

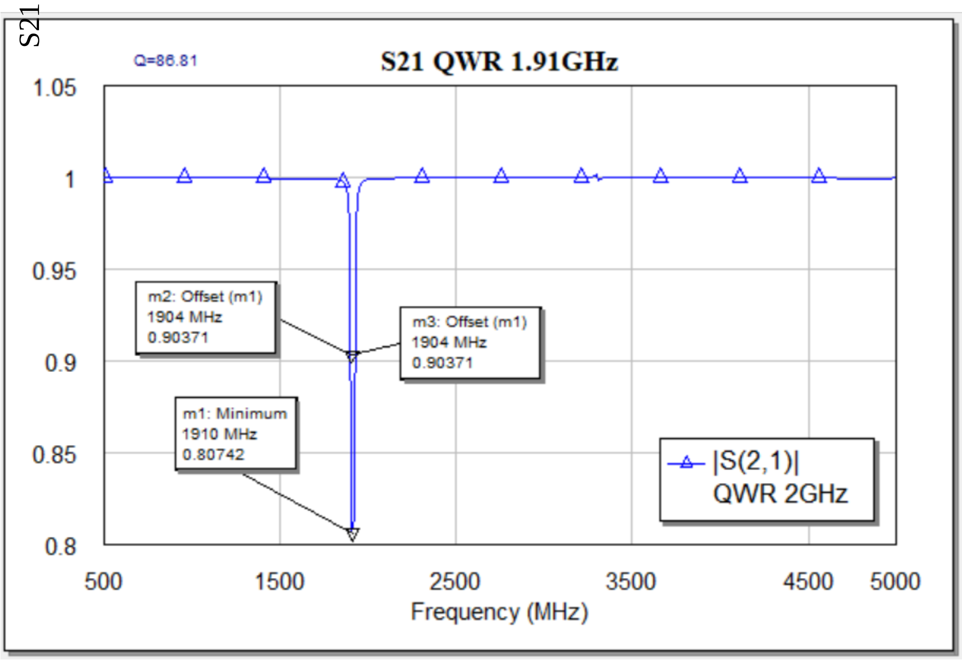

(b)

Figure 5.3: (a) A schematic showing the design of the quarter wave resonator. The resonator is simulated using a simple design with no folds or curves initially to determine the frequency through the simulation. (b) A graph showing the S21 parameter for the quarter wave resonator. It shows a resonance at 1.91GHz with a quality factor of 86.81. Markers m1-m3 are placed to determine the full width half maximum which is a measure of the quality of the resonator.

A quarter wavelength resonator which comprises of a short on one side and an open circuit condition on the other side creates a resonance condition when the wavelength of the electromagnetic wave is one quarter the resonator length for the initial resonance. Further resonances occur when multiples of a half wavelength in addition to a quarter of a wavelength equals to the resonator length.

This type of design was considered but compared to the low impedance resonator it would not have a very large current as there is not a constriction and it is also not as localised. The half wavelength is also a viable alternative but was not thought to be the best solution for one defect area coupling to one resonator in the strongest manner possible.

The resonator was designed by first approximating the capacitance of a design using the conformal mapping technique (R. Igreja, 2004) which involves looking at the geometry of the capacitor and comparing the design to a parallel plate capacitor. The transformation to make the two plates of the capacitor parallel and not inline with each other is the conformal mapping. From this technique the capacitance of the interdigitated capacitor can be measured.

In addition to the conformal mapping techniques, an approximation of the inductance was found by looking at the simulated S21 measurements which represents the power going into port 2 as a percentage of the power going into port 1.The S21 parameter has a sharp drop at the resonance frequency due to the power being lost to the environment from port 1 as shown in the Figure 5.3. The design was then constructed in Microwave Office with the feedline and the resonance frequency was obtained. Final amendments were made to the design to get the desired frequency. The design and the simulation of the first iteration of low impedance resonator are shown in Figure 5.4.

(a)

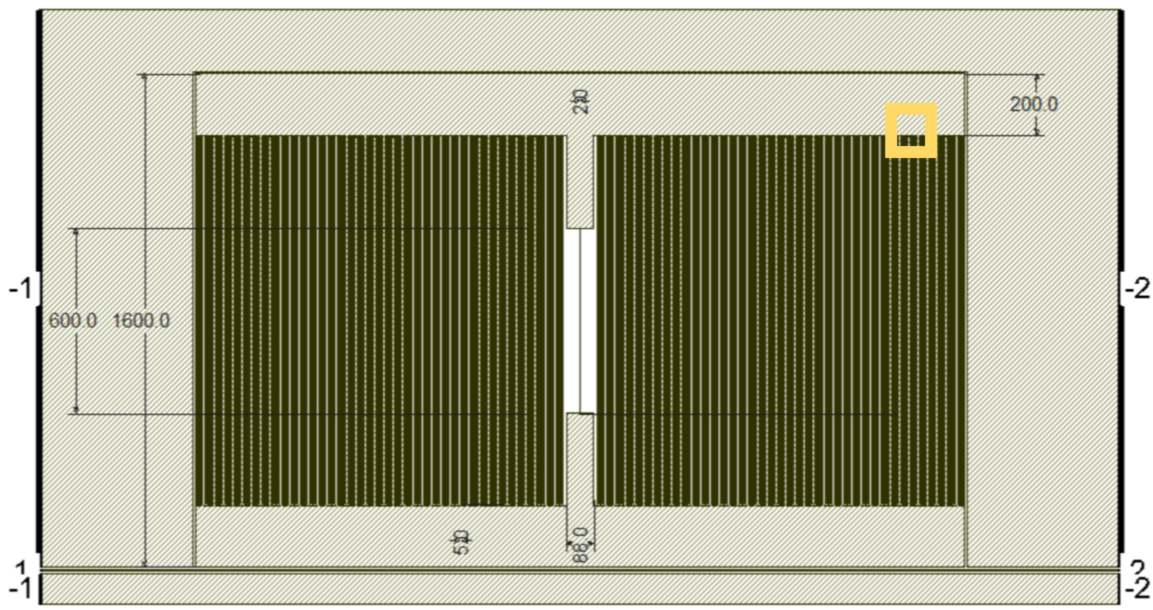

(b)

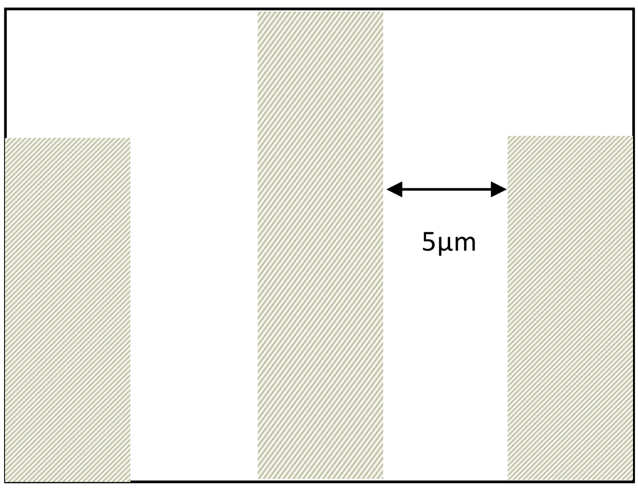

(c)

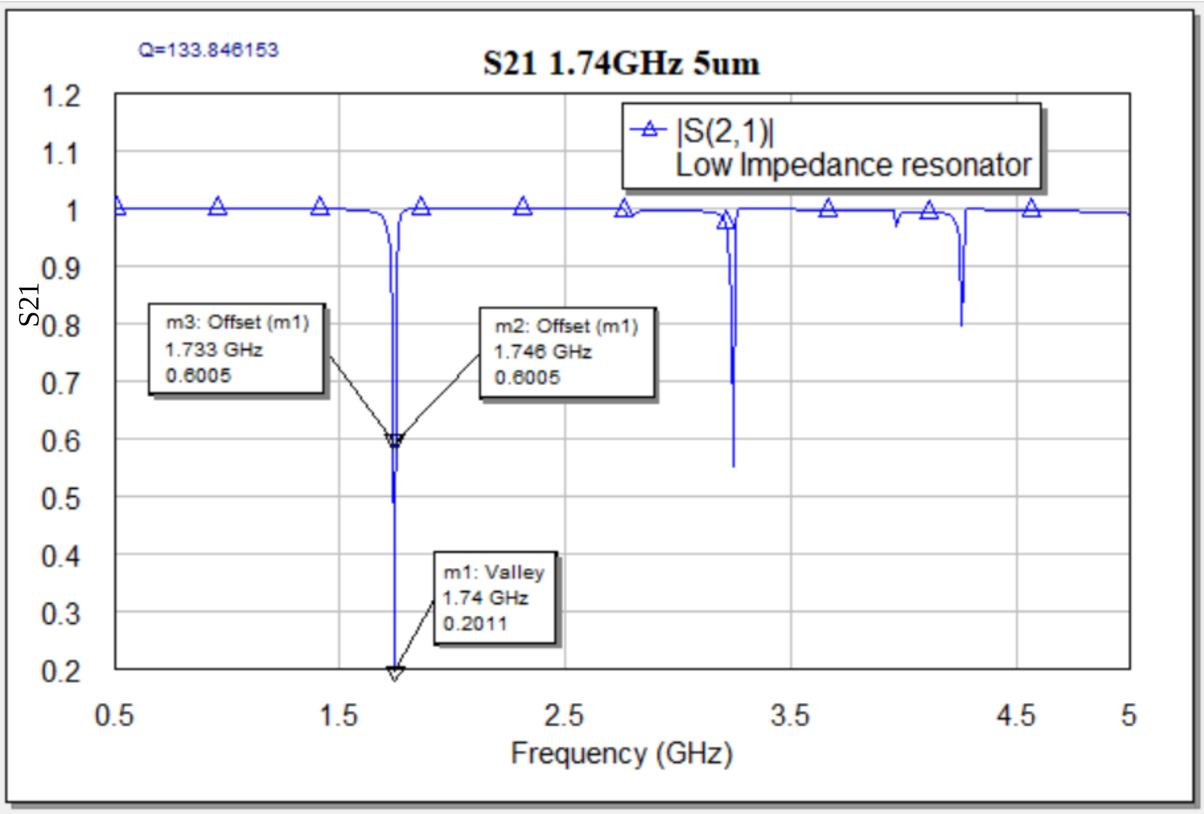

Figure 5.4: (a) A schematic showing the initial design of the low impedance resonator which becomes part of D3 with all dimensions in microns. The design consisted of a central inductor and two interdigitated capacitors on either side of the resonator (b) An inset of (a) where there is a yellow square which shows the dimensions of the interdigitated capacitor (c) A graph showing the S21 parameter of the low impedance resonator with a resonant frequency of 1.74GHz and a quality factor of 133.85. Several resonances are seen in the simulation which were subsequently seen in the experiments.

5.3 Current Flow

The current that flows through the central inductor can be found by looking at the heatmap that is produced in microwave office and shown in Figure 5.5 which gives the current when the input is 1mW.

In addition to this, the current when there is no input can be approximated by finding the inductance which is found by using the fact that the capacitance of the resonator is a known quantity, and after the resonator is simulated through microwave office, the resonant frequency will be known.

The inductance could also be calculated using the conformal mapping technique by considering the capacitor as the ground plane and proceeding with the conformal mapping calculation, but it was better to use the simulation as it would provide all the couplings and give an answer which may not be fully accurate but would give some guidance to the measurable quantities.

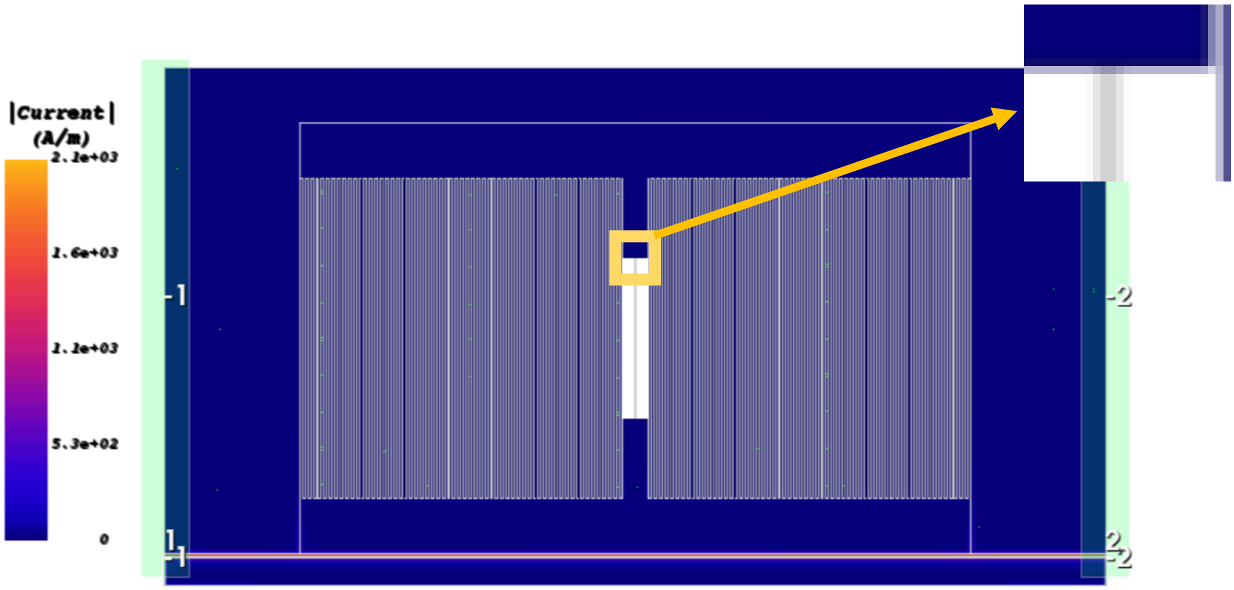

***Figure 5.5**: The heatmap of the simulation of the current through the resonator of D3 using Microwave Office. The inset shows the area of interest which is the inductor where the current is particularly high. The current was high in the inductor and low in the capacitor so the magnetic field is high around the inductor.*

As the capacitance and resonance frequency are known, the inductance can be easily calculated as described above. After knowing the inductance, the resonator can be thought of as a harmonic oscillator and when all the energy is in the magnetic field, the current can be calculated for when the harmonic oscillator is in its ground state. Using this method, the current is found to be around 9.65nA for the 1.74GHz resonator and an inductance of L = 6.185nF using Equation 5.1.

$$E_{min} = {I_{min}}^2 L = \frac{hf}{2} \rightarrow I_{min} = \sqrt{\frac{hf}{2L}} = 9.65nA$$

Equation 5.1: Equation for Emin.

Once a current is obtained, the magnetic field can be found by using a model of a thin rectangle with current passing from one short side to another, and when looking at the cross section this is given as:

$$B_x = \frac{\mu_0 I}{p} = \frac{\mu_0 I}{2\pi r + 2a}$$

Equation 5.2: Equation for Bx.

Where r is the distance away from the wire in the radial direction and a is the length of the short side of the rectangle with μ_0 being the permittivity of free space and I being the current.

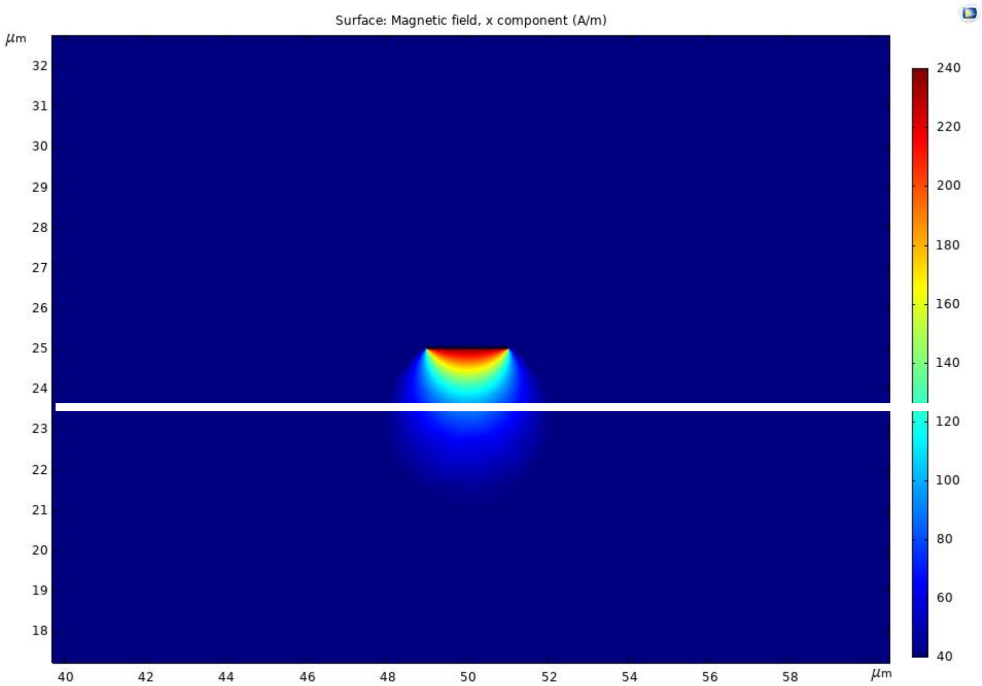

Figure 5.6: Schematic showing the magnetic field on one side of the 50nm tall and 2um wide inductor with the color range limited to 40A/m which was produced using COMSOL. The white line represents the surface of the resonator, in particular the inductor. The magnetic field can be shown to be large close to the surface of the inductor with the field strength dropping off further from the resonator.

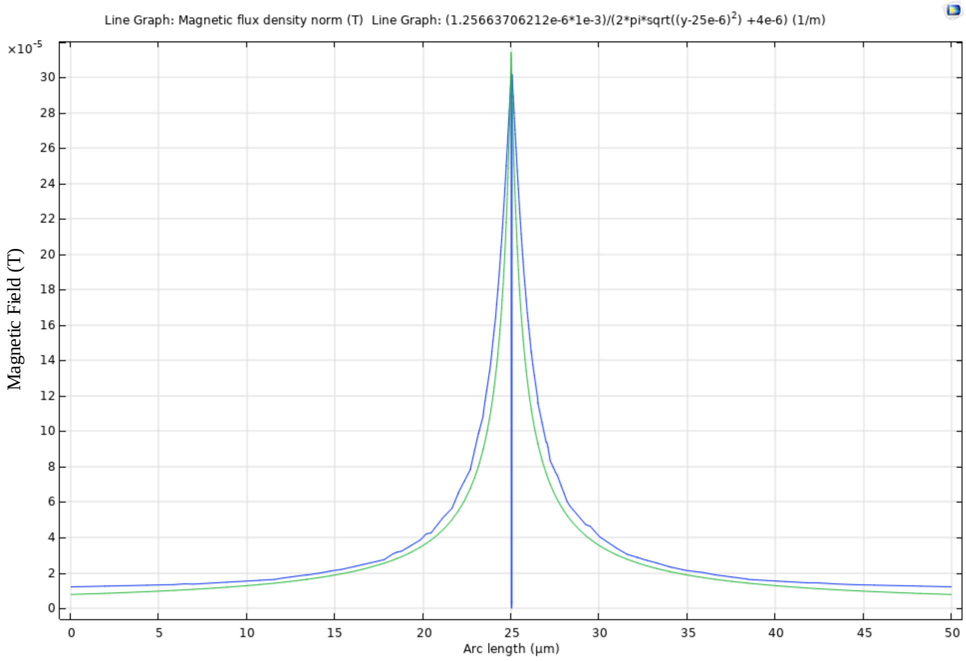

Figure 5.7: Graph showing the magnetic field straight down the middle of the simulation area from 0µm – 50µm on the y axis with the data from the simulation in blue and the equation $Bp = \mu_0 I$ in green where p is the path integral around the wire and I is the current enclosed. The simulations match the equation closely as the green line (calculation) is very close to the blue line (simulation).

To verify the magnetic field is correct and the expressions are correct to a certain factor the model was built in COMSOL and the results can be seen in Figure 5.6 and Figure 5.7. This gave a very close correspondence to Equation 5.2. The blue line in the above figure shows the simulation results and the green line shows the theoretical model using the equation $\boldsymbol{Bp} = \boldsymbol{\mu_0 I}$ .The green line fits the simulated results very well which shows the equation can be used to simulate the magnetic field around the inductor.

At larger distances from the inductor the results do deviate. This disparity is maybe due to the edge effects of the inductor, but the effect is more likely due to the finite thickness of the inductor used in the COMSOL model. This finite thickness of the inductor also causes a dip at the middle of the inductor in the simulated results but not in the theoretical model.

This effect can be easily rectified by putting limits to where the equation is valid, namely outside the inductor. There do seem to be bumps in the blue line which displays the simulated results, and this is attributed to the simulation error, as there is a limit set to how much the result should converge between simulation steps before the simulator moves to the next calculation.

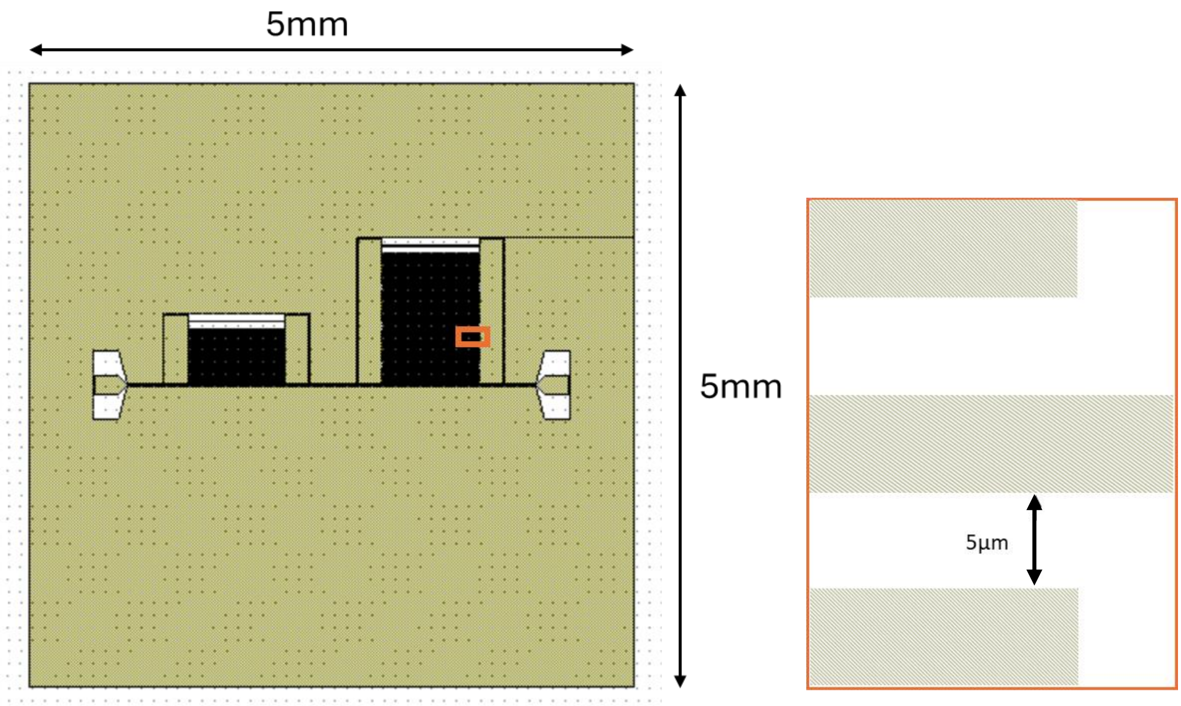

Figure 5.8: A schematic showing the alternate design of the low impedance resonator D1 with the orange box zoomed in to show dimensions. There are two resonators with the inductor on the top of the resonator and the capacitor on the bottom. The tuning of the frequency can be done by increasing the size of the capacitor by adding more lines in the interdigitated capacitor. The orange box on the left is zoomed in on the right. The spacing between the lines in the capacitor is shown.

The initial design of the low impedance resonator was a good starting point but had some design features built in which may have hindered the ability of the spins to interact with the resonator in an isolated way. An alternate design was made to address these issues, and the schematic of this design can be seen in Figure 5.8. It shows the capacitor being parallel to the coplanar waveguide instead of perpendicular to the waveguide with the inductive wire being on top of the resonator as far away from the waveguide as possible instead of in the middle of the resonator.

One of the advantages of the alternate design could be the increased electrical isolation of the inductor from the waveguide due to the coplanar waveguide being as far away from the inductor as possible. This could in the future mean that if spin active material is placed on the waveguide, signal from the waveguide would not adversely affect the spins as much. Another advantage of the inductor being on top of the resonator instead of in the middle of the resonator is thought to be the increase in electrical access to the inductor for further changes. Implementing a tuning element such as squid (O. Suchoi, 2010) with its control lines would be easy to implement on the alternate design as there is space on top of the inductor.

The alternate design also has one big capacitor instead of two capacitors, and this makes it easier to make design changes to change the frequency as it is easier to ensure the design is symmetric when changing the frequency.

Further changes were made to the existing design such as increasing the spacing on the sides of the resonator which could increase the quality factor due to lower coupling to the ground plane.

Resonator design D2 differs from resonator design D1 as it has extra spacing on the sides of the resonator. Similarly, design D4 has an extra spacing on top of the resonators compared to design D3.

All the final designs of the resonators, coplanar waveguides and bond pads have extra features such as the bond pads having a gradually increasing spacing to the ground plane to ensure there is not a change in impedance. The waveguides also end on a strong coupling to the ground plane which is thought to decrease the amount of back reflection from the bond pads.

6 Resonator Production

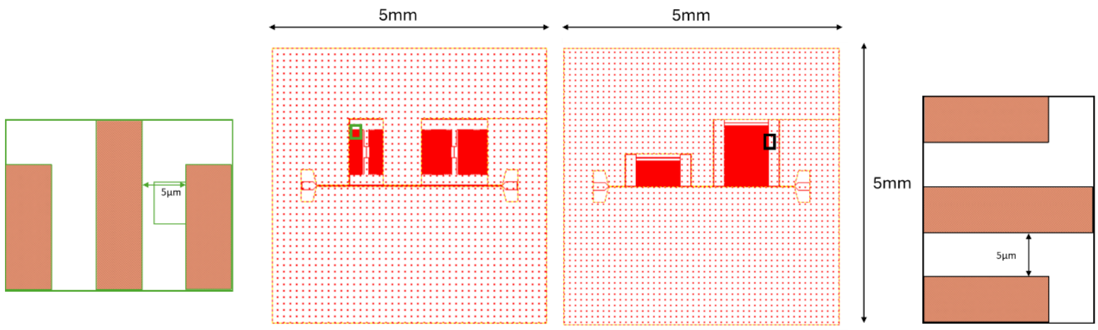

***Figure 6.1: A schematic showing the designs of the low impedance resonators D3 on the left (with a green box which is zoomed in for dimensions) and D1 on the right (with a green box which is zoomed in for dimensions) in the production format.* The chip size was 5mm x 5mm which is shown in the figure.**

The final designs to be produced consisted of four designs. They were named D1,D2, D3 and D4. The first and second designs D1 and D2 had two interdigitated capacitors with a inductor in the middle as shown on the right hand side Figure 6.1 with the difference between D1 and D2 being that there was extra space on the top of the resonator for design D2 so there was metal layer which would isolate the resonator slightly more from the ground plane.

Designs D3 and D4 looked similar with the overall design having one interdigitated capacitor with an inductor on top as shown on the right-hand side of Figure 6.1. The difference between D3 and D4 being D4 had an extra space on either side of the resonator to isolate the resonator from the ground plane.

Bothe the resonators has two resonators with the smaller footprint design having a designed resonance at 3GHz and the larger resonator designed to have a resonance at 2GHz.

The final designs for the resonator had to go through a final formatting to ensure it was ready to produce the resonators. The format is a simplified layer by layer approach mainly for the optical mask and is shown in Figure 6.1. In the conversion process, sometimes errors are made, and it was important to ensure that the resonator design changes were again amended to reflect the true design. One of the reasons was that in the conversion process some of the details could be lost, which then must be reintroduced once the conversion is complete.

The resonator production included deposition of 70nm of high-quality sputtered niobium on a substrate of Si which could be A-plane Sapphire, followed by a lithography step which involved spin coating of 80nm of PMMA onto a substrate and curing it followed by a dry etching step into the silicon which meant the full etch was 150nm in total.

Usually, e-beam exposures have hundreds of micro coulombs per cm squared and is used for the etching step although in the case of this resonator an inert ion etch was used. The etching gas used was argon with an inductively coupled plasma to provide a non-reactive etch with an accurate pattern. The pressure in the chamber is around 20mTorr, with the power being around 700W. The etch time is determined by the etch rate which is calculated by the machine as this is a variable which changes with the condition of the machine, although for this etch the time is expected to be less than 30s. This results in a RF design which is printed onto niobium. The design was done by myself and the etching and deposition was done inhouse by the NPL team, mostly by liaising with the inhouse expert who detailed the steps used in the processes.

Other methods could be used such as electron beam etching, or a lift off process. The quality of the films is important in determining the quality factor of the resonator which is produced. Impurities could affect the superconductivity of the material which in turn could result in a poor-quality resonator.

Niobium was chosen due to its ability to withstand high magnetic fields and remain superconductive. Also, its high superconductive temperature allows niobium to become superconductive easily. Some studies have explored vortex pinning by the introduction of a pattern of vias to enhance the resonators ability to withstand high magnetic fields. Niobium titanium nitride and niobium nitride may also be suitable materials for superconductive materials for resonators.

Annealing may change the film properties which could lead to advantageous or disadvantageous changes to the property which is mainly caused by a change in grain size of the material. The deposition technique and parameters used in the deposition also has a large effect on the superconductivity of the film and hence the quality of the resonator.

7 Measurement design

There is a myriad of experiments which can be done using resonators or spin systems. They are mainly composed of continuous wave and pulsed measurements which both require vector network analysers.

The primary mode of action is through sending a drive signal to the device under test and the return signal is analysed. The return signal is sometimes composed of a real and imaginary component. These components are then compared to theory which can determine whether the models used are correct.

The resonator can be tested by a continuous wave drive S21 measurement. The resonant frequency manifests itself as a sharp dip in the S21 magnitude parameter. This is because when the resonator is resonant it absorbs the energy of the incoming drive pulse.

The resonance is only present when the niobium is superconductive, and as the resonator has a high quality factor, the frequency range has to be highly focussed on the resonator frequency range to observe the dip and fit an equation to determine the parameters.

Magnetic field can also be applied to the resonator whilst the experiment is run to see the effect on resonant frequency and quality factor. The resonance frequency shift is thought to be due to the change in inductance due to the magnetic field.

The magnetic field is usually applied perpendicular to the plane in which the film lies. The application of a magnetic field can cause vortices which affect the superconductivity and the quality factor of the resonator. There is a specific magnetic field at which the superconductivity diminishes, and thus the resonators quality factor diminishes, which is an important parameter, as it determines the amount of Zeeman splitting which can be provided and controls the frequency range with which the resonator can operate and couples to the spin active component near the resonator.

One of the key measurements that can measure the coupling factor is the S21 measurement. This requires continuously driving the microwave power and sweeping the frequency and changing the magnetic field to obtain an S21 measurement. Measurements using the continuous wave power methods were performed to determine the resonant frequency of the resonators. A dip in the S21 measurement shows the resonant frequency.

The S21 measurement of a coupled system, namely the coupled spin and resonator system can be modelled using a simple model based upon the coupling between two harmonic oscillators, where one of the harmonic oscillators represents the spin system and gives the equation:

$$\omega = \frac{\omega_a + \omega_r}{2} \pm \sqrt{g^2 + \frac{(\omega_a - \omega_r)^2}{4}}$$

Equation 7.1: Equation for omega.

Where g is the coupling factor and ω_a and ω_r are the bare defect and resonator frequencies respectively. With $\omega_a = \frac{2\pi S\mu_B g_s B}{h}$, and B being the applied magnetic field which changes the energy level spacings. Equation 7.1 does not take into consideration any losses and cannot replicate real life exactly. For this input-output formalism is required for considering the more detailed equation which details losses related to the environment.

There are also other measurements which could be done which include pulsed measurements. The details of some of the pulse sequences are shown below in Figure 7.1, Figure 7.2 and Figure 7.3.

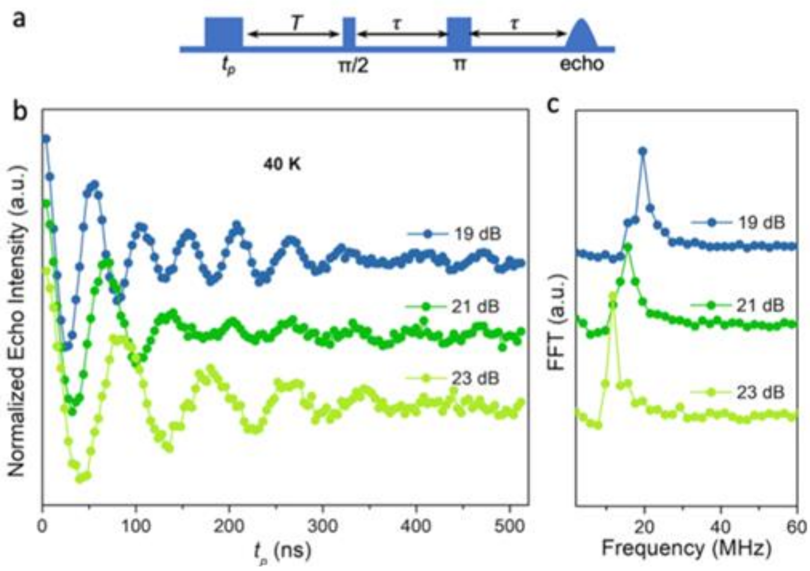

Figure 7.1: Graph showing a typical Rabi pulse sequence used with the results shown below. The top section shows the pulse sequence which is an initial pulse followed by a pi/2 pulse and a pi pulse after which an echo is shown to occur. The bottom section shows the pulse intensity with differing initial pulses tp and their fourier transform is shown on the right. (J. Lopez-Cabrelles, 2021)

Pulsed experiments may be of interest to find the T1 and T2 coherence of the defects, and Rabi oscillations can also be shown by either changing the power or duration of a pulse before a pi/2 pulse and keeping the time separation t fixed between the pi/2 pulse, the second pi pulse and the final measurement as shown in Figure 7.1 above. There should be an oscillation between the states and thus the signal obtained.

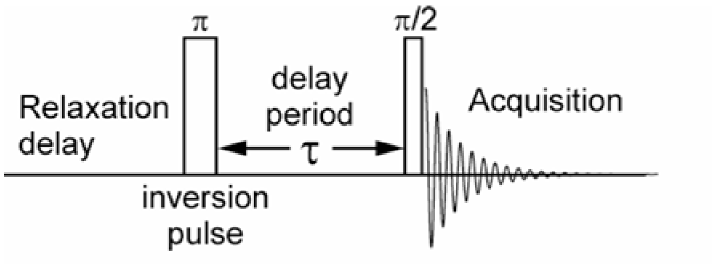

Figure 7.2: Diagram showing the pulse sequence of a T1 measurement. The is an initial relaxation delay followed by a pi inversion pulse and a delay after which a pi/2 pulse is shown followed by an acquisition. (Majumdar, 2015)

Similarly, to measure T1 one would have an initial pi pulse followed by a time T which is varied which is followed by a pi/2 pulse and an acquisition as shown in Figure 7.2. One can clearly see if the time

T is zero it would just give a rotation of 3/2 pi which is equivalent to pi/2 which should give a strong signal.

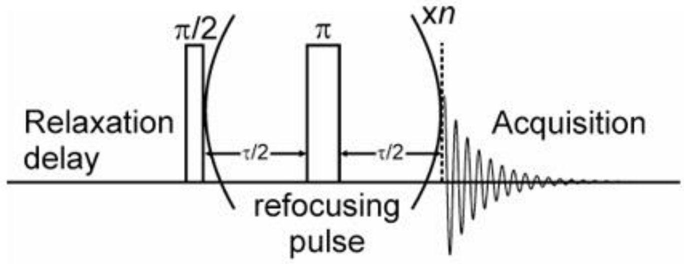

The CPMG pulse-sequence for measuring T_2. The number of times the echo is repeated, n, should an even integer.

Figure 7.3: Diagram showing the pulse sequence of a T2 measurement. A relaxation pulse is followed by a pi/2 pulse after which xn refocusing pi pulses and an acquisition occurs. (Majumdar, 2015)

To measure T2 one would start with a pi/2 pulse followed by a time t which is changed and then apply a pi pulse and wait a further t seconds. One can gain extra data points to fit the decaying exponential for T2 by adding another pi pulse instead of measuring the echo after a further time t as shown in Figure 7.3.

Further developments in the measurement scheme could involve performing one qubit operations on a spin ensemble but this would require a further radiofrequency magnetic field which could be provided by a resonator that is at 90 degrees to the original one.

To create and manipulate two qubits they would need to be coupling between the two qubits. This may require better hardware such as a tuneable resonator which could be made by adding Josephson junctions to the current design and trying to add some bragg reflectors to minimise loss.

8 Testing Equipment and method

Testing of the resonators required a dilution refrigerator and other testing equipment including a vector network analyser and some amplifiers. The dilution refrigerator cools down the equipment to under 10K. This is vital to create the conditions which allows the niobium to become superconductive. The stages are shown in Figure 8.1 to provide a flow diagram which provides an overview.

Figure 8.1: Figure outlining the cooling stages of a dilution refrigerator. There is an initial expansion cooling followed by evaporative and dilution cooling stages.

The dilution refrigerator can be thought of as a combination of different cooling methods which cool the object sequentially. There are various different designs of dilution refrigerators, an example of a common type can be seen in Figure 8.2.

The first stage usually comprises of expansion cooling which includes a compressor and an expansion valve and expansion of the gas. The second stage of the cooling is usually evaporative cooling. This is where the gas is evaporated, and the interface has a reduction in temperature due to the hot particles being removed from the liquid from evaporation. The last stage of the cooling is usually the dilution cooling. This is when the helium -3 moves from one stage to the other which is an endothermic reaction.

8.1 Dilution refrigeration

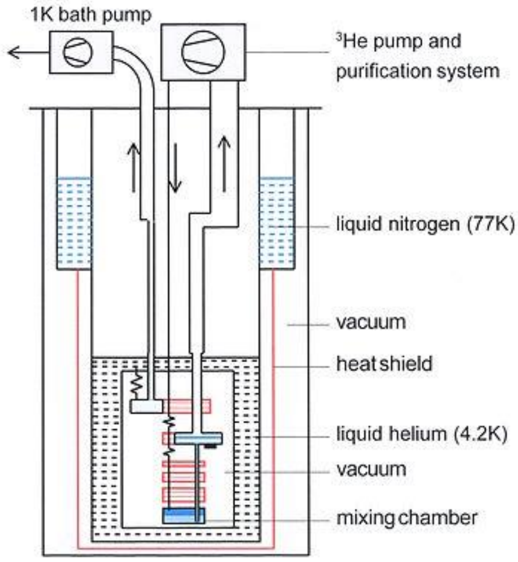

Figure 8.2: A schematic of a dilution refrigerator which is similar to the one used in the experiment. The schematic shows helium being pumped into the system into the mixing chamber where the cooling occurs. Additional heat shielding and a vacuum is added to the system to reduce heat losses.[1]

The first cooling process is due to the joule expansion of a gas which is then subsequently compressed by a compressor and expanded again at the expander. In this manner, the place where the expansion occurs cools considerably.

This is because when a gas expands, the gas reduces in temperature. This can be done by helium gas or by nitrogen gas where the expansion part is thermally coupled to the helium part. This is usually done in pulses and the equipment is usually known as a pulse tube cooler.

The second stage occurs when the helium liquefies. The liquid helium is composed of helium-3 and helium-4 and when a vacuum is created on top of the liquid helium in the still, the helium-3 evaporates and this in turn cools down the liquid.

This is due to the hotter parts of the helium mixture being removed which in turn reduces the overall temperature of the gas. This evaporation is usually improved by having a vacuum above the liquid gas interface by placing a pump above the interface which enables the evaporation to occur easily. The helium-3 can be reintroduced at the other side of the helium bath.

The third stage occurs in the liquid helium. The liquid helium is made of two phases, the dilute phase and the concentrated phase. The concentrated phase is nearly 100% helium-3 and the dilute phase is around 6% helium -3.

As the helium-3 from the still evaporates, the helium-3 needs to be replenished in the dilute phase to maintain this equilibrium of roughly 6% of helium-3. This is done by helium-3 flowing from the

[1] https://en.wikipedia.org/wiki/Dilution_refrigerator#/media/File:Dilution_refrigerator01.jpg

concentrated phase to the dilute phase. This process of the helium flowing from the concentrated phase to the dilute phase is endothermic and thus the phase boundary layer cools.

The part of the fridge which usually contains the two phases is known as the mixing chamber and thus the mixing chamber cools down even further. The concentrated phase is connected to the top of the fridge through a pipe with heat exchangers which allows the heat to be dissipated as the helium-3 reaches the bottom of the fridge.

The cooling components are very sensitive to heat exchange. For this reason, the fridge is kept at a vacuum to reduce the heat exchange due to convection. Multiple layers of reflective metal encase the cooling components along with the test and control equipment. This is to reduce radiative heat exchange from affecting the experiment and the temperature of the fridge.

The components inside the fridge are specially designed to ensure that the thermal expansion and contraction of the system is possible without damaging the fridge. This also means that the fridge bolts are all tightened to a specific torque to ensure that the overtightening or under tightening of the fridge does not damage any components of the fridge.

The fridge is usually leak tested once the fridge is closed, under vacuum. This is because a small leak could cause a lot of thermal exchange with the surrounding air once cooled down and could result in the fridge not being able to reach its operating temperature or damage to the internal parts of the fridge, sometimes due to the components overworking to reach the required temperature.

A leak test can be done by spraying compressed air around the seals and looking for small changes in the pressure on the various pressure gauges inside the fridge. If a leak is found, the relevant seal and component may need to be reassembled or replaced and tested again.

The fridge cooldown is usually monitored very carefully using the internal temperature gauges and is done in a controlled manner by the automated process with various software interlocks. The different pressure gauges and temperature sensors control the valves which slowly cool down the fridge.

The helium is usually first cleaned of impurities by going through cold traps and is then slowly introduced to the fridge in the cool down process. The process usually takes hours and sometimes may need to be stopped if everything is not within the normal operating conditions when the fridge is being cooled down.

8.2 Experimental Equipment

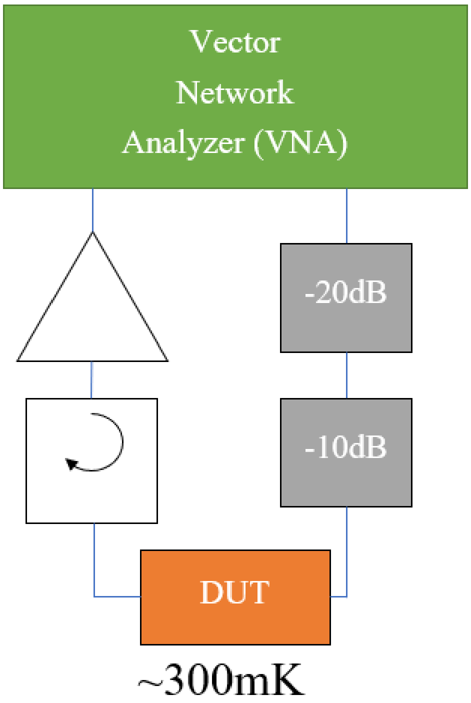

Figure 8.3: Schematic of the experimental setup. A network analyser is connected to the DUT through cables shown as solid lines and attenuators shown in grey. There is a circulator and an amplifier to amplify the signal which then goes back to the vector network analyser.

The experimental equipment used with a simplified version shown in Figure 8.3 included a vector network analyser which had a frequency range of roughly 100Hz to 14GHz and some coaxial wires to the fridge and subsequently to the device under test.

The signal from the device under test went through a circulator and subsequently went to a HEMT amplifier and out of a fridge to a low noise amplifier. This signal was picked up by the vector network analyser and the S21 measurements were subsequently taken.

The vector network analyser is a RF measurement device which measures the RF power and other components like the real and imaginary component of the input radiofrequency. The vector network analyser also outputs a drive power.

The drive power is usually very low to avoid saturating the resonator. When the power is outputted and measured from another port on the network analyser, a comparison between the input and output power can be done. This is what the S21 measurement is. It compares the output power to the input power and provides this information which is then saved.

The output power goes down the coaxial cable which is usually a low loss version to ensure there is minimal power loss. Time delay reflectometry is often used to ensure the line has no breaks inside the cable and to ensure all the connections are properly connected. This provides an initial diagnostic tool to ensure the electronics are working properly.

A radio pulse is sent down the wire and the reflection back to the port is seen at different times corresponding to different points down the wire where the signal is reflected. In this manner, if the cables and connections are faulty, or there is a sudden change in impedance, the signal tends to be reflected and thus the faults in the cable can be identified before installation, and perhaps even after installation.

The components that are outside the fridge such as the low noise amplifier and the cables are usually at room temperature and do not experience a huge temperature change before and after installation when the fridge is cooled. However, the coaxial cables inside the fridge can experience severe thermal changes when the fridge is cooled down.

Due to this reason, the coaxial cables are made of specialised materials such as titanium and copper beryllium which provide the correct thermal load and thermal conductivity for the section of the fridge which it is installed in.

Some extra considerations are needed to ensure that the cables in the fridge are superconducting to ensure there is a minimal loss of signal. Also, due to the requirement of a vacuum being present inside the fridge, the cables should not be made of materials which outgas. If objects inside the fridge outgasses, the inside of the fridge may not be able to reach a very low-pressure vacuum.

The testing components inside the fridge were mainly the high electron mobility transistor which amplifies the signal after passing through the device under test. The power to the amplifier is delivered through DC cables from the outside of the fridge. The signal needs to be amplified because the noisy environment outside the fridge may subdue the signal.

The background noise from the amplifier to the device under test can be reduced by inputting a circulator. The three-port circulator is connected to ground on one of the ports and connected to the device under test on the other port with the remaining port connecting to the amplifier.

The signal from the device under test goes to the amplifier, whilst the back signal from the amplifier is grounded to ensure that the device under test is not affected by the amplifier. The circulator can be affected slightly by the magnetic field, and care should be taken to ensure that the circulator is not magnetised. This can be achieved by using a mu-metal shielding on the circulator, or ensuring that the circulator is not close to any strong magnets.

A magnet is often used in the dilution refrigerators to perform experiments. The magnet is usually a superconducting coil and thus can provide a very high current and a very high magnetic field. There are dangers which are mainly due to the high amounts of magnetic energy sometimes being directly deposited into the internal components and sometimes, when some part of the coil becomes non superconductive this can cause highly localised heating and the magnetic field can be destroyed in this way.

The magnet is usually initialised slowly by flowing current in the coil and in some cases the coil is short-circuited, and the power supply is turned off. This can allow the magnet to operate without any power since the current is superconductive and does not lose energy.

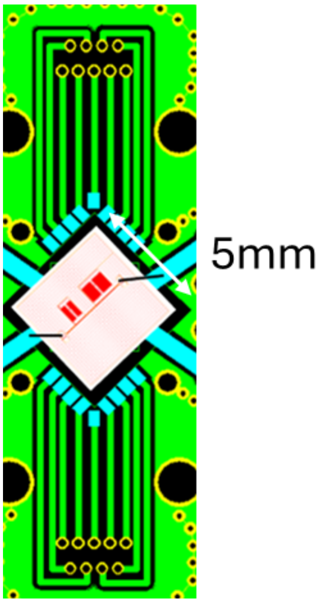

Figure 8.4: The amended PCB design for use in the fridge. The PCB is shown in green with the chip shown in red in the middle with the black lines connecting the chip to the PCB.

Some of the equipment which was used in the experimentation had to be specially designed, such as the chip shown in the figure above. This was due to the chip design being too large for the original PCB which is the red square in the middle of the PCB in Figure 8.4.

The design changes included rewiring the DC connectors at the top and bottom of the chip and enlarging the chip area alongside the rotation and movement of the RF connectors. The original fittings and functionality of most of the connectors were kept the same. This was helpful as it meant that major changes to the placeholder were not required.

Although minor alterations were made to the placement of the four RF connectors to allow for the larger chip. The material of the chip was a 0.8mm R04003C material with a 1 oz finished copper coating. The materials were chosen to enable the chip to be used in vacuum conditions.

The sample holder in particular needed amending due to a change in the PCB which holds the sample. Small changes were made to an original sample holder to ensure the same setup could be used and so large changes did not have to be made, and to keep the costs down. The sample holder only had to be drilled in four places with a precision drilling machine.

The hardware side of the experiment setup requires careful planning and building, which requires a lot of manual tasks such as screwing things together and ensuring bolts are tightened. The software side of the experimental setup is mainly composed of sending commands to equipment to ensure the equipment is interfacing correctly and making small adjustments to the setup, such as installing communication cables to setup communication channels.

Once all the equipment is interfaced correctly, and is communicating correctly, software programs are written to perform small test experiments. These are crucial as it provides a baseline for the system, and can be compared to other experimental setups which act as a reference.

Once the experimental setup is baselined, the experimental data can be produced. Some manual data can be produced and initially analysed for initial results. The main experiments can also be done manually, but because the manual data can take a long time to obtain, many experiments are automated.

The automation program is usually a coding-based program such as LabView. The program is interfaced with the equipment, sometimes through another program and a test automated experiment is run. This is usually to baseline the automated software. Once the automation program is baselined, the automated experiments are started.

One of the key factors in the experimental design is the health and safety aspect. Procedures are written to perform processes in a safe manner and one of the key factors in ensuring the experiment is done safely is the remote control of the experiment.

The remote control of the experiments allows the experiment to be done with minimal disturbances and if something does go wrong in the experiment, ensures people are not in the vicinity of the experiment. It can also provide a means of easily monitoring the experiment and acting quickly and safely if required.

9 Testing of the resonators

$$T_{21} = A_1 + A_2(f\text{-}f_r) + \frac{A_3 + A_4(f - f_r)}{1 + 4Q^2(\frac{f - f_r}{f_r})^2}$$

- A_1 determines the height of the overall background
- A_2 determines the slope of the overall background
- A_3 determines the deep the resonance is
- A_4 determines the skewedness of the peak
- Q is how sharp the peak is
- f_r is the resonance frequency of the peak
- Taken from a thesis written by Jiansong Gao (Gao, 2008)

Equation 9.1: The equation used to fit the data from the resonators.

The data was taken from the vector network analyser and analysed. Predominately, the data included the real and imaginary components of the S21 measurements. The magnitude squared of the S21 measurements can be compared to theory and a skewed gaussian can be fitted to the data, and the frequency and quality factor could in turn be determined. Example data and an initial guess of the fit are shown in Figure 9.1.

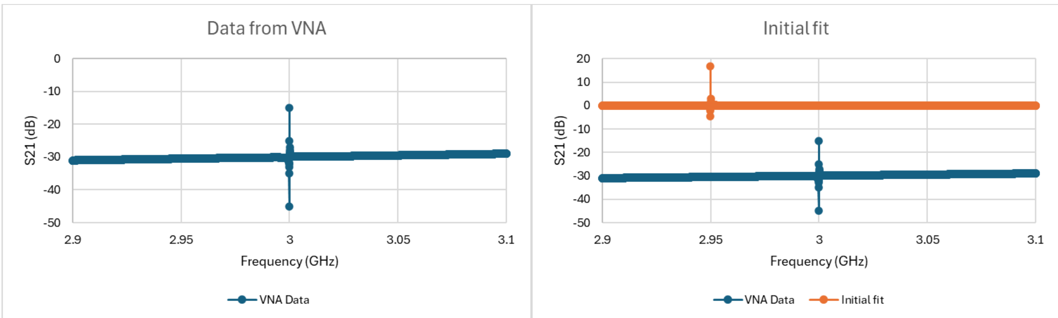

Figure 9.1: Graph showing the raw data to be fitted (left) and an initial fit. The initial fit is shown as an orange line with the data shown in blue.

For the resonators tested, the skewed Lorentzian equation was used to fit the data. This is a common way to fit resonator data as it provides various extra terms as can be seen in Equation 9.1 which considers the background noise and some of the effects of the coaxial cables.

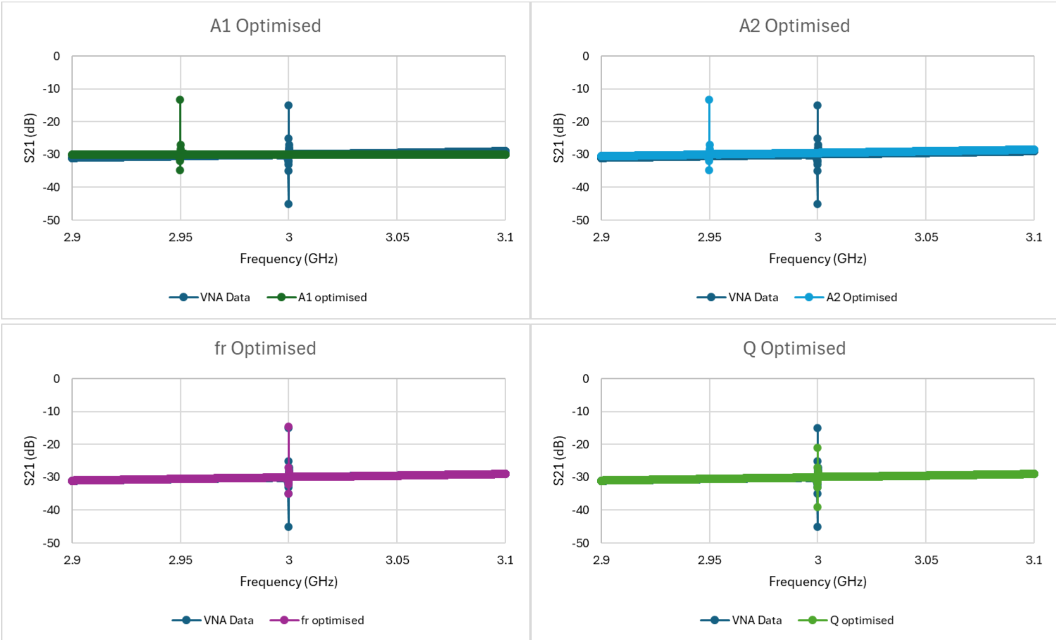

Figure 9.2: Graphs showing A1 optimised (top left), A2 optimised (top right), fr optimised (bottom left) and Q optimised (bottom right). The fit closely resembles the data more after the fitting for each parameter. When A1, A2 and fr are optimised, the data is very similar to the fitting curve.

The method of fitting the data was by changing the data to the correct format and then fixing all the parameters initially and setting a reasonable initial parameter for each of the variables. The next step was to let A_1 vary and minimise the residual, which is the difference between the fitted curve and the data. A_1 mainly affects the offset of the curve in the y-direction or magnitude. The A_2 value was usually optimised by allowing A_2 to vary. This allowed the slope of the background to fit the slope of the fitted curve. f_r and Q were normally optimised next. The iterations of the optimisations of these fit parameters are shown in Figure 9.2.

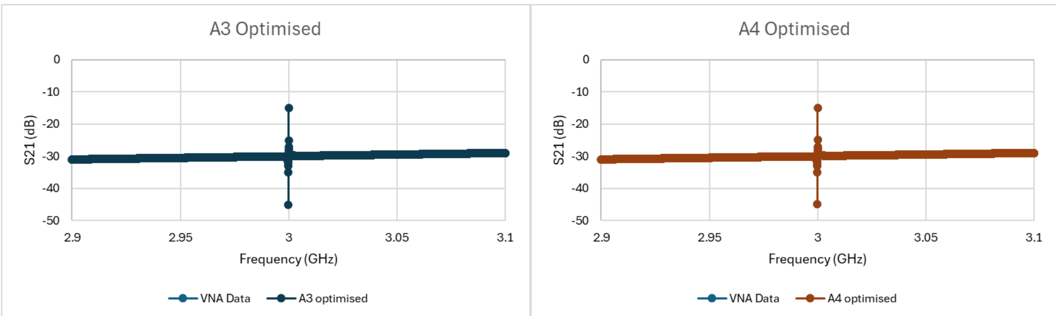

Figure 9.3: Graphs showing A3 optimised (left) and A4 optimised (right). A3 and A4 optimisation have small effect on the fit but does make the fit match the data more accurately.

A_3 and A_4 were optimised last and example of A3 and A4 being fit are shown in Figure 9.3. Sometimes the resonance did not get fully optimised, and this was sometimes due to the fact that even though A_3 and A_4 are optimised, if f_r and Q are not fully optimised the curve would not fit properly. To overcome this challenge A_3 and A_4 are optimised, and then f_r and Q are optimised again in a cyclical manner. In this way A_3, A_4 , f_r and Q quickly minimises the residual. Once all the values are roughly optimised, all the parameters can change in the final optimisation step which allows the residual to be reduced over a few optimisation cycles.

An alternative way to fit the data is to fit the real and imaginary components using the circle fit method (S. Probst, 2015) (M. S. Khalil, 2012). This uses a different equation to the one outlined above and uses a specific model for the capacitance and inductance to calculate the theoretical parameters.

This in practice may allow a more precise value for Q and the resonant frequency f_r but is difficult to implement due to the amount of data needed near the resonant frequency. If enough data points are not taken near f_r, the fit can be difficult to implement and may result in an incomplete fit and the wrong fit values for Q and f_r along with the other parameters measured in the model such as the coupling parameter.

When a spin system is added on top of the resonators and the resonant frequencies do not differ by much and the system couples, there is a different equation which may be used for the S21 parameter (V. Ranjan, 2013) (A. K. V. Keyser, 2020) (Palacios-Laloy, 2010) (Casper, 2015). This equation is based on input output theory and treats the incoming wave and resonator dynamics in a very different way to those stated above.

10 Results

The experiments started with the reference resonator to baseline the system and to ensure the results are similar to those measured elsewhere. The experiments then went on to investigate the influence of input power on resonance frequency and the quality factor of the resonator. This led to the final experiments which looked at the frequency and quality factor of the designed resonators to confirm that the simulations and the designs obtained the correct values in real world testing.

10.1 Reference Resonator

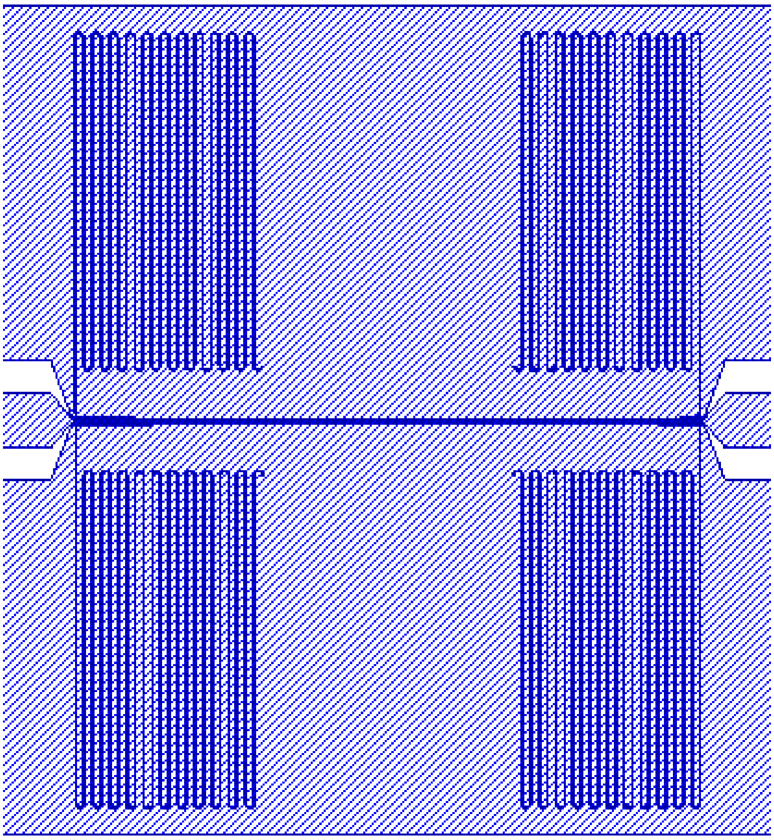

Figure 10.1: Schematic showing the design of the test resonator. There are four quarter wavelength meander resonators each with different coupling lengths.

Initially, the testing equipment was referenced using a reference resonator which is shown in Figure 10.1. The resonator is composed of four quarter wave resonators with a similar length but with different coupling lengths which refer to the length of the resonator which is parallel to the feedline.

The reference resonator was referenced for the resonant frequency and the quality factor and extra experiments were done to determine how the resonator performs when the input power is increased as well as in the presence of a magnetic field. This provides a baseline, the measured values of which is given in Table 10.1 to compare some of the characteristics of the low impedance resonator.

Magnetic Field (T)	Frequency (GHz)	Quality Factor	Reduced Chi Squared
0.01	2.54505	1163.1496	3.07485e-7
0.02	2.5275	1284.00533	1.38223e-7
0.03	2.5185	1144.6053	4.11793e-7
0.04	2.508	901.73345	4.56222e-8
0.05	2.4975	795.59736	7.64122e-9
0.06	2.4892	661.41325	1.6426e-9
0.07	2.48	549.79502	4.80294e-10
0.08	2.471	459.86027	4.08484e-10
0.09	2.46	354.43113	2.9358e-10
0.1	2.4534	356.86209	3.66983e-10

Table 10.1: Table of the resonances of the test resonator with differing magnetic fields. The quality factor and the reduced chi squared are also shown. The magnetic field seems to have an effect on the quality factor and the resonant frequency.

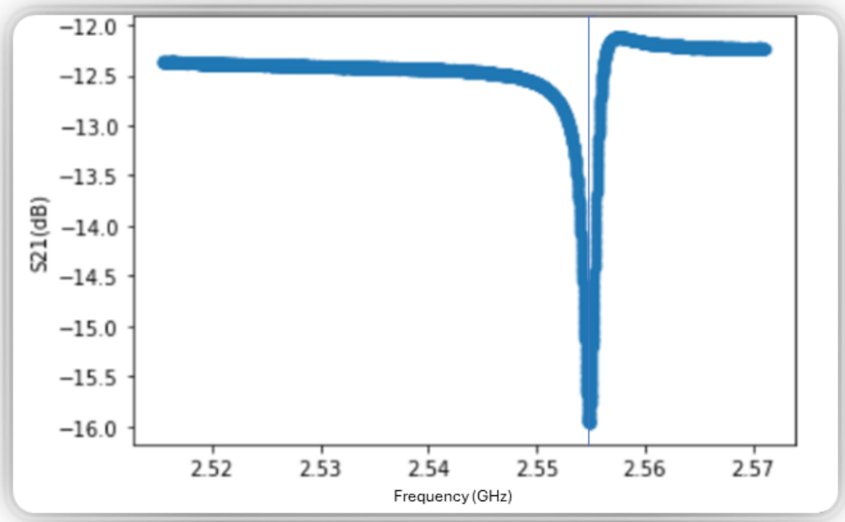

Figure 10.2: Data provided about the reference resonator Sample B. There is a resonance shown in the figure at 2.54GHz which is shown as a trough in the figure.

The reference resonator had a resonant frequency at around 2.54GHz with a quality factor of around 1000 at 0.01T as shown in Figure 10.2. This is comparable to what was provided about the reference resonator which has a resonant frequency of around 2.55GHz.

The data measured against the reference data baselined the fridge hardware and the RF measurement system and allowed for further experiments to be performed with the confidence that the components were performing in the correct manner.

The data measured also provided some reassurance that the resonator is a reliable reference as the frequency had not changed by much and that the resonance was still there which meant that the reference resonator was robust and able to survive being remeasured after a long period of time.

10.2 Resonator Input Power dependence

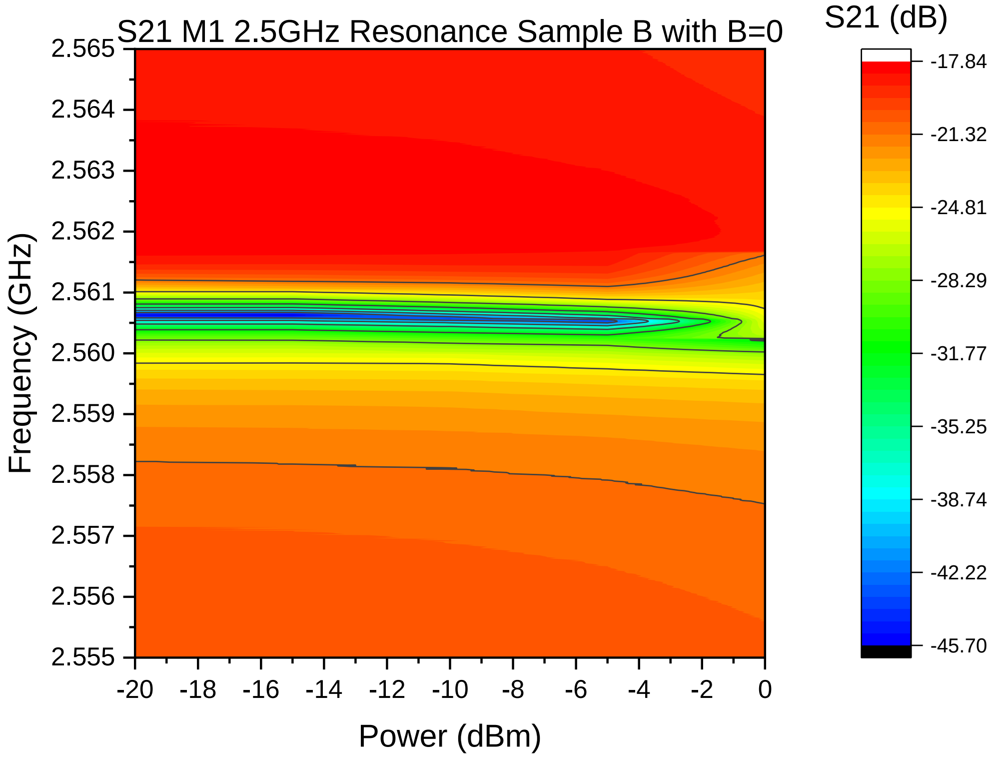

Figure 10.3: Input power dependence and S21 response of the reference resonator B. The contour graph shows the frequency changing with differing powers and the S21 values increasing with increasing amounts of input power. This amounts to a broadening of the resonance peak.

The input power dependence of the reference resonator was of interest due to the need to calibrate the input power to ensure the proceeding resonators were not damaged by too high a power. Also, the frequency response was measured to look for any changes and as shown in Figure 10.3 no discernible changes were seen.

The frequency does not seem to depend on the input power. On the other hand, the quality factor does seem to change. This is seen in Figure 10.3 as a broadening of the peak as one looks at the graph from the left-hand side to the right-hand side which corresponds to a low power of -20dBm to a high power of 0dBm.

This power dependence on the q factor may be due to resonator saturation. When there is too much power stored in the resonator it seems to become very lossy. For this reason, most experiments were done at either -10dBm or -20dBm.

This value for the input power is not an absolute value which goes to the device under test because some of the input power is inevitably lost in the coaxial cables and some of the other apparatus. The input power nevertheless gives a good indication of the amount of power going into the resonator and gives a good upper limit to the amount of power entering the device under test.

10.3 Reference Magnetic Field dependence

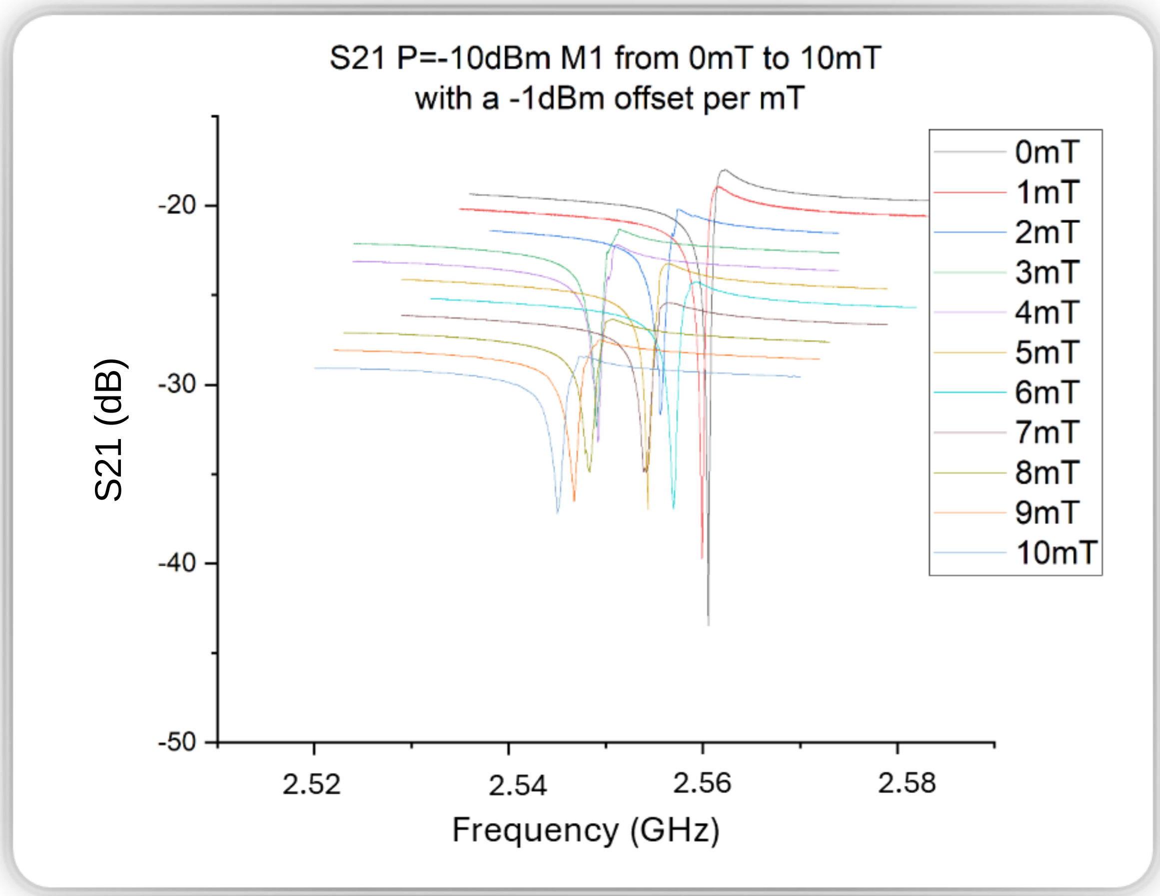

Figure 10.4: S21 response due to an external magnetic field on Sample B. The magnetic field was varied between 0mT to 10mT in 1mT steps. With increasing magnetic fields, the resonance shifts to lower frequencies and the resonance broadens.

The magnetic field dependence of the resonator in sample B can be clearly seen in the Figure 10.4. At higher magnetic fields the resonant frequency seems to decrease. This decrease could be attributed to the effects of a kinetic inductance which affects the resonator frequency, the equation which govern these are shown in Equation 10.1, Equation 10.2 and Equation 10.3. The quality factor of the resonator also seems to decrease as the magnetic field is increased. This could be due to the deterioration of the superconducting capabilities of the film.

$$\frac{1}{2}(2m_e v^2)(n_s A l) = \frac{1}{2}L_k I^2$$

Equation 10.1: governing the kinetic inductance of a superconducting object.

$$\boldsymbol{I = 2evn_sA}$$

Equation 10.2: Equation relating the current I to the velocity and change of an electron.

$$L_k = \frac{m_e l}{2e^2 n_s A}$$

Equation 10.3: Equation governing the kinetic inductance of a superconducting object.

The kinetic inductance is a property which is defined by the inductance caused by the kinetic energy of the superconducting pairs. The pairs are the two electrons which have an attractive interactive term to make them superconductive.

Each superconducting pair has a kinetic energy associated with the movement of the pair through the material and this is linked to the kinetic energy as shown in Equation 10.3. The equation can be rearranged for the kinetic inductance as shown in the bottom of Equation 10.3. As the magnetic field increases, the number of superconducting pairs n_s decreases and causes the inductance L_k to increase, which in turn reduces the resonant frequency of the resonator.

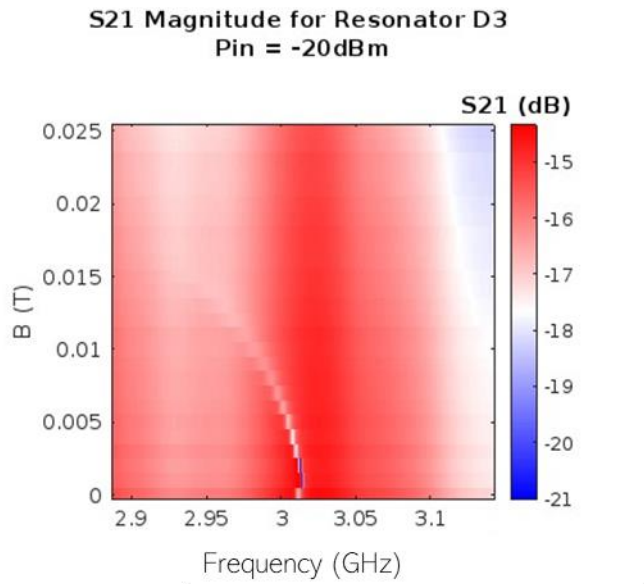

Figure 10.5: S21 response of resonator design D3 with varying applied magnetic field. The graph shows that the frequency shifts to lower frequencies with higher magnetic fields and the resonance broadens. At around 0.017T the resonance has broadened significantly.

The S21 response of the designed resonator D3 can be shown in Figure 10.5. The resonance can be found at around 3GHz which is the designed frequency. This sharp resonance is a typical feature of a superconductive resonator and shows that the design on D3 does indeed produce a resonator system.

Looking at Figure 10.5 and focussing on the colour graph, the magnetic field dependence can also be seen, and the resonator quality factor drops at around 0.017T which could be improved by producing the resonator on a higher quality film.

The characteristic curve of the resonator which shows how it behaves in increasing magnetic fields shows that there is not a sharp drop off but a smooth drop off. This is of interest, as this shows that the spin resonator system could be stable as there is not a sharp drop off but a more subtle drop in the quality factor due to the fading effect and a subtle shift in the frequency due to the magnetic field as the resonance moves more to the left-hand side.

Resonator	Frequency (GHz)	Magnetic Field
D1	3.13	0mT
D1	1.93	1mT
D2	1.93	0mT
D3	3.03	0mT
D4	3.03	0mT

Table 10.2: Frequency and the corresponding magnetic field measurement value of the resonator D1,D2,D3 and D4. The frequencies are close to 3GHz and 2GHz which were the design frequencies at close to zero magnetic field.

The other resonators designs were also measured, and the resonator D1 was measured with both the fundamental frequencies of the two resonators measured and analysed at 3.13GHz and 1.93GHz as shown in Table 10.2, which isn't too far off the 2GHz and 3GHz the resonators were designed for.

Some of the resonator designs were only measured for one of the resonators such as D2 which showed a resonance at 1.93GHz and D3 and D4 which both showed their resonance frequencies at 3.03GHz.

A quick measurement of the Q factors showed that D4 had a higher quality factor than D3 and this could be due to the spacing on top of the resonator which isolates it from the ground plane and could reduce energy loss through the top of the resonator. Similarly, resonator D2 had a higher quality factor than D1 showing the same is possible with spacings on the sides of the resonator which can reduce energy loss.

The results of the resonator data show that the frequency can be reliably simulated and produced with a high level of certainty. The resonator could go on to in the future couple to spin active components which are in the range of the frequency of the resonator.

11 Discussion

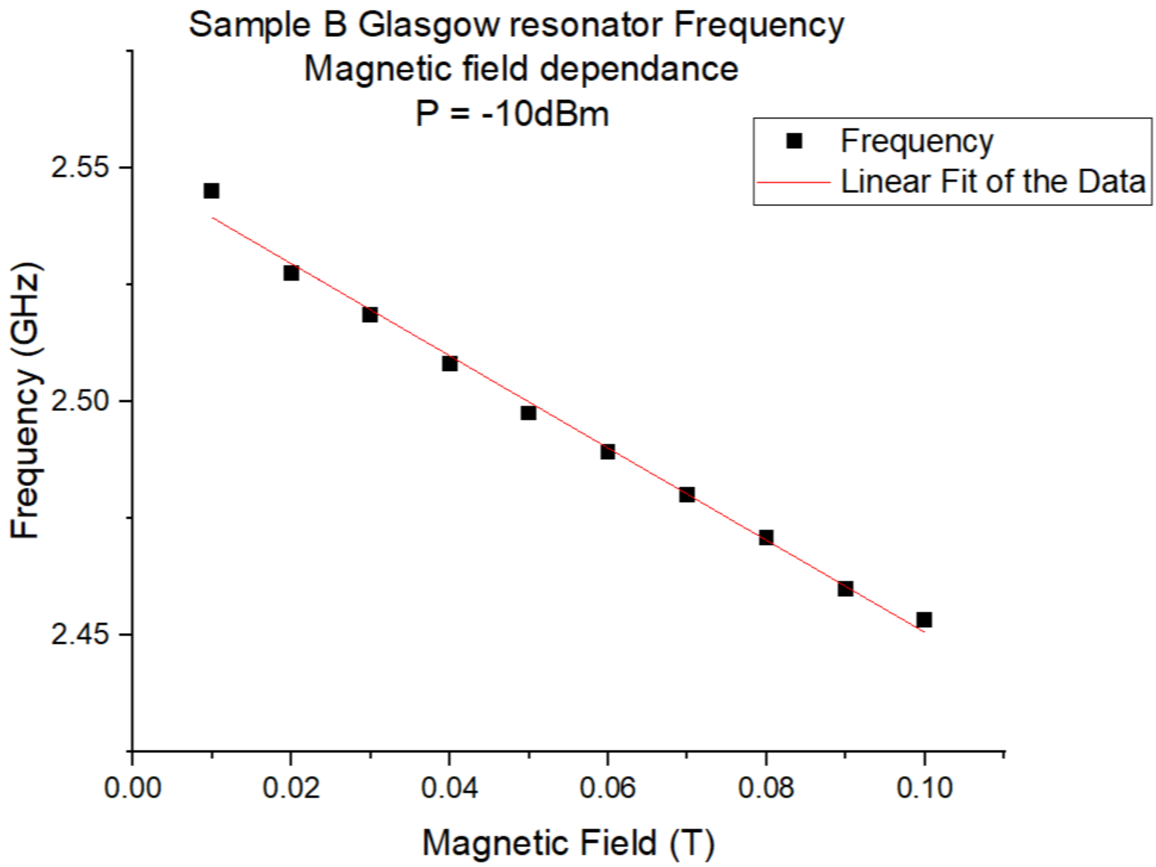

Figure 11.1: The frequency response of sample B due to an external magnetic field. A clear relation can be found with increasing magnetic field reducing the resonant frequency in a linear manner.

11.1. Resonator magnetic field interaction

The resonator results show that the resonant frequency shifts due to the magnetic field as shown in Figure 11.1 and not due to the power, and that the quality factor is affected by both the magnetic field and the input power. The mechanism for the resonant frequency is thought to be because of the kinetic inductance, and the shift could be useful in trying to tune a resonator into having the same resonant frequency as a resonator.

The resonator frequency shift is not always linear and perhaps different resonator designs have their different characteristically different frequency response to the magnetic field. The frequency shift could also be different for different materials.

This could warrant further investigation by annealing the existing resonator designs in a reactive environment to change the film material and hence its film properties such as its kinetic inductance. For example, if the resonators were annealed in a nitrogen environment to change the film into a niobium nitride film, the kinetic inductance may change to a higher value (S. Frasca, 2023).

The resonant frequency of the resonator at zero magnetic field and at increasing magnetic fields may be of interest and prove that the material is or is not a key factor in determining what the resonator's resonant frequency is at zero magnetic field and whether the film dictates how the resonant frequency of the resonator changes with the application of a magnetic field and how this may change the characteristic magnetic field against frequency curve.

The addition of a similar or a dissimilar layer of material on top of the design with the same features may provide additional information to determine whether the capacitance remains the same but the inductance does not, and could provide clues as to how to make the resonator designs more resilient to magnetic field changes.

The addition of a layer may be more difficult to implement in practice because the first layer may develop an oxide layer which may prevent the first layer from adhering properly to any additional layers which could be overcome with a short etching step.

Dissimilar layers may require an adhesion layer which may make electrical contact more difficult. The addition of an additional layer nevertheless could provide some clues to determining what affects the magnetic field resilience of the resonator.

11.2. Resonator design and experimentation

The fact that the measured resonant frequency was very close to the designed and simulated resonant frequency provides evidence of the reliable way in which RF resonators can be designed for a certain resonant frequency and produced, and in the future the models could be made more accurate by feeding in the measured frequency of the resonators and readjusting for the offset.

Resonators of different frequencies could also be made by changing the size of the capacitor as demonstrated in the experiments above. The relatively small footprint of the resonators compared to quarter wavelength resonators mean that the size of the chip does not have to be very large to reach the lower frequencies for a resonator, and because of the symmetry and relative simplicity of the design compared to quarter wavelength resonators, the simulations are not as complicated, which allows for the simulations to be done with less computation time.

The resonator results of D1 and D2 differed in the Q factor but not the frequency. This is crucial as the coupling to the ground plane was decreased by increasing the gap to the ground plane. This increase in Q factor due to the change in the gap can be exaggerated by increasing the gap to the ground plane even more and looking at the changes in the Q factor to see if the Q factor increases more.

If the frequency remains the same but the Q factor does increase, it could show that the spacing is important and that the Q factor decrease is due to the energy being lost from the resonator to the ground plane.

The different resonators D2 and D4 are similar conceptually but have a different design. They both worked and the S21 dip was seen in both at their characteristic frequency. The design of D2 has potential benefits over D4 due to the simpler design with only one capacitive element and one inductive element rather than having two capacitive elements and one inductive element as seen in D4.

Due to this change, only the size of one capacitor needs to be changed for a frequency shift in the design of D2, whereas for the D4 design both the capacitors need to be changed and look symmetrical. In addition to this, to add a SQUID (O. Suchoi, 2010) to the inductor to make the resonator more tuneable, the element and the control lines can easily be added to the inductor on the top of design D2, whereas for the D4 design something more complicated would have to be designed and implemented.

The inductor being very far away from the coplanar waveguide also lends itself well to being isolated from noise in the coplanar waveguide in design D2. More iterations to the design D2, would make the design D2 a lot more favourable to the D4 design.

11.3. Resonator Spin Coupling

The resonator and its ability to withstand a certain amount of magnetic field is crucial to building a spin coupled system. For example, for the V2 vacancy in 4H-SiC, 15mT is required to go from 70MHz to 500MHz for the v2 line which goes from S=+1/2 to S=+3/2.This gives 430MHz/15mT = 0.0286GHz/mT or 34.88 mT/GHz.

So, if a 1.5GHz resonator was designed, a magnetic field of 52.33mT would be required. And for the resonators that were designed and tested which had the resonant frequency at roughly 2GHz a magnetic field of 69.77mT would be needed to bring the spin system and the resonator into resonance.

If the resonator was designed to have a smaller footprint with a higher frequency of 2.6GHz, a magnetic field of 90.70mT would be required. These magnetic fields are a little high for the resonators that were tested, and the resonator would most likely not have a high enough Q factor for the effects of the V2 spin system to be seen.

For the divacancy defects in 4H-SiC, specifically the PL1 (P6b) which is a (hh) defect with a splitting of 1.336GHz the requirements on the ability to withstand stronger magnetic fields may be less stringent.

The change in the resonance frequency and zeeman splitting can be calculated because at 35Gauss (3.5mT) the resonance is roughly 1.425GHz. So, this gives a change of 0.089GHz/3.5mT, 0.025GHz/mT or 39.3mT/GHz. The requirements for a 1.5GHz resonator would be the ability to withstand a magnetic field of 6.45mT which would be feasible from the experiments shown above.

For a 2GHz resonator, a magnetic field of 26.12mT would be needed, which may mean that the resonators designed above may not be able to withstand the magnetic field required to see the coupling effects between the defect and the resonator. Lastly, a 2.6GHz resonator and a magnetic field of 49.71mT would be required to see the coupling effects using a 2.6GHz resonator.

To allow for the coupling to be seen, the resonators designed would need to be designed for a lower frequency. This would mean a larger footprint on the chip. Other methods could be investigated for the coupling to be seen, which could include making the resonators using a niobium nitride film or making the resonator out of a better-quality material.

The substrate could also be changed to reduce the losses into the substrate. Design features could also be added which could include the addition of vortex pinning sites which may increase the magnetic field resilience of the film (C. Song, 2009). The resonators in this experiment were not perfectly coupled, and as such optimising the coupling could also being some benefits.

This would require more measurements to be made to determine the current state of the coupling. The real and imaginary components of the S21 measurement would be required and fit using the circle fit method (A. Megrant, 2012).

The coupling would be decreased by moving the resonator away from the feedline or reducing the length of the feedline parallel to the resonator to reduce the coupling capacitance. Conversely, the coupling would be increased by moving the resonator closer to the feedline or increasing the amount of the feedline which runs parallel to the feedline.

The production of the vacancies has its own challenges. Firstly, the 4H-SiC is a material which may come with its own intrinsic defects (J. Sumarkeris, 2005), and although this can be useful as it can provide some defects without any process steps, it could hinder the spin coupling, and further unwanted effects down the line may be due to these defects. Low defect SiC can be produced but tends to be more expensive.

The defect production process begins with the simulation of the ion implantation as shown earlier on in the text. The simulation provides an estimation of where the defects may be, and allows the energy of the incoming ion to be chosen for a certain application.

Lower power implants tended to create vacancies on the surface of the material, whereas the higher energy defects create vacancies further inside the material. The defects also tended to be silicon vacancies due to the binding energy being lower than that of carbon in the simulation, and this is thought to translate well in real life.

Laser annealing is thought to enhance some of the properties of the defects (Gupta, 2016) (Akl, 2018) and could possibly enhance the optical properties of the defects (H. K. Lin, 2015). This may be due to crystal healing, or due to the defect being changed.

The annealing process is thought to allow the defects to migrate, with different defects migrating at different temperatures. This in turn allows some defects to combine and make new defects, or allows the defect to vanish, by finding a place in the crystal where it would ideally be.

Different processes occur at different rates, and the careful control of temperature is important in determining which processes occur. In the annealing process, sometimes a carbon capping layer is added to the silicon carbide (L. Kuebler, 2024). This is because when the silicon carbide is heated, some of the silicon evaporates compared to the carbon which evaporates slower due to the lower binding energy of silicon. To mitigate this, a layer is added on top of the silicon carbide to eliminate this evaporation.

Many models can be created to try to replicate how the spins couple to the electromagnetic field, but one of the main ways this was done was by looking at the magnetic field profile and looking at how different energies of implantations with certain dosages would affect the coupling rate.

A more complicated version would consider the saturation of the spins, which could look at the photon to spin ratio at certain points in the crystal. If the ratio is more than one, the spins would be saturated, and if this was less, then the spins are not saturated. The ratio could be a metric to determine the effective coupling. The coupling could be reduced if there are not enough photons to interact with the spins and thus although the spins are present the effective coupling could be lower.

The models to show the resonant behaviour of the coupled system can be derived using the principles of quantum mechanics. The model used show the splitting and the overall structure of the resonances and is based on the coupling of two oscillators. A more rigorous derivation including losses can be derived using input output formalism and considers various loss mechanisms.

More complicated experimentation such as the demonstration of certain quantum states being stored in the resonator, or the spins could be done with extra equipment. One experiment would be the transfer of quantum information from a qubit to the spin system and back to the qubit for measurement again.

The experiment could be done at various dwell times in the spin system and the qubit, to show how the information may be stored for longer in the spin system. Some initial experiments have indeed been done using the NV spin system and an extension of this research to show that it could work in 4H-SiC would be a useful measure of the method's universality.

Currently, a quantum computer is usually based on superconducting qubits. Although, optical qubits may be a possibility in the future (Pieter Kok, 2007), the large systems that are needed may mean that optical quantum computing may not be a feasible option until the optics become smaller, and possibly chip scale.

Spin quantum computing may be rather bulky too and may require loads of magnets and other equipment to ensure that the gates can be implemented. The positive side of spin qubits are the long decoherence times compared with superconducting qubits.

A hybrid system of a superconducting qubit along with some spin component may be very useful in increasing the coherence time of the qubit (Bhattacharyya, 2019) (Xiaobo Zhu, 2011). The exchange of quantum information remains a challenge between two different technologies for quantum computing, namely, spin and superconducting qubits.

Perhaps, with some tuning and greater understanding of the interface between superconducting electronics and spin systems, some progress could be made in better designing the interfaces. And this would enable this technology to be optimised and hopefully ready for implementation, maybe the technology to make higher quality thin films and closer control of the implantation would also be useful in this regard.

Localised annealing could also help in providing some measure of control when producing the intended defects and engineering the interface for the exchange of quantum information (W. Hsu, 1999).

12 Conclusion

The simulation of the defect generation and theoretical coupling showed a new method in which the coupling to a spin ensemble can be simulated and theoretically measured to a specified resonator. If the coupling matches the theory and can be shown to be strong compared to the losses, a quantum memory could be made which could be coupled with a qubit system to increase the time for qubit calculations.

The results from the experimentation and the project point to a conclusion which shows a capability to design and produce a low impedance resonator to a specific frequency. The resonators had a designed frequency of 2 and 3GHz and this is what was seen when the resonance was measured with the measured resonances being 1.93GHz, 3.03GHz and 3.13GHz. This capability could be used in the future to couple to spin active components within the resonator's frequency range or the resonator could be designed for the specific spin system.

Future work could include the introduction of a frequency tuning element to the resonator, such as the integration of a Josephson junction and some control electronics onto the thin film. In addition to this, the resonator could be made more resilient to external and stray magnetic fields by the introduction of vortex pinning sites into the substrate. The resonator could be of a higher quality by decreasing the amount of energy loss to the ground plane by perhaps reducing the capacitive coupling to the ground plane through the gap from the resonator to the ground plane although this remains a theory and more experiments would be needed to show this in practice.

The implantation and annealing of the silicon carbide could be tweaked and amended to provide a reliable way to produce certain intended defects, and the coupling could be experimented and analysed to ultimately try to create a quantum memory for superconductive qubits.

13 References

A. K. V. Keyser, J. J. (2020). Pulsed electron spin resonance of an organic microcrystal by dispersive readout. *Journal of Magnetic Resonance, 321*(106863). doi:10.1016/j.jmr.2020.106853

A. Kawasuso, H. I. (1997). Vacancy production by 3MeV electron irradiation in 6H-SiC studied by positron lifetime spectroscopy. *Journal of Applied Physics, 82*(3232). doi:10.1063/1.36530

A. Megrant, C. N. (2012). Planar superconducting resonators with internal quality factors above one million. *Applied Physics Letters, 100*(113510). doi:10.1063/1.3693409

A.Bienfait, J. P. (2016). Controlling spin relaxation with a cavity. *Nature, 531*(77).

Akl, A. S. (2018). X-ray studies: Co2 pulsed laser annealing effects on the crystallographic properties, microstructures and crystal defects of vacuum-deposited nanocrystalline ZnSe thin films. *CrystEngComm*, 7120-7129.

Bhattacharyya, K. M. (2019). Hybrid spin-superconducting quantum circuit mediated by deterministically prepared entangled photonic states. *AIP Advances*, 115111.

C. Song, T. W. (2009). Microwave response of vortices in superconducting thin films of Re and Al. *Physical Review B*, 174512.

Casper, P. (2015). *Characterization of microwave devices for multiplexing quibit readout.* Thesis, ETH Zurich, Quantum Physics Lab. Retrieved from https://qudev.phys.ethz.ch/static/content/science/Documents/semester/Patrik_Casper_SemesterThesis_150714.pdf

D. Christle, A. F. (2015). Isolated electron spins in silicon carbide with millisecond coherence times. *Nature Materials, 14*, 160-163.

D. I. Schuster, A. P. (2010). High-cooperativity of electron-spin ensembles to superconducting cavities. *Physical Review Letters, 105*(140501).

Gao, J. (2008). *The physics of superconducting microwave resonators.* Dissertation, California Institute of Technology. doi:10.7907/RAT0-VM75

Gupta, Z. S. (2016). Laser annealing of silicon surface defects for photovoltaic applications. *Surface Science*, 344-349.

H. K. Lin, K. C. (2015). Effects of laser annealing parameters on optical and electrical properties of ITO/metalllic glass alloy bi-layer films . *Nanoscale research letters*.

H. Malissa, D. I. (2013). Superconducting coplanar waveguide resonators for low temperature pulsed electron spin resonance spectroscopy. *Review of Scientific Instuments, 84*(025116), 025116. doi:10.1063/1.4792205

J. F. Wang, Q. L. (n.d.). On-demand generation of shallow silicon vacancy in silicon carbide. Retrieved from https://arxiv.org/ftp/arxiv/papers/1810/1810.11252.pdf

J. Liu, Z. X. (2020). Confocal photoluminescence characterization of silicon-vacancy color centers in 4H-SiC fabricated by a femtosecond laser. *Nanotechnology and Precision Engineering, 3*(218).

J. Lopez-Cabrelles, L. E.-M.-G.-A. (2021). Near Isotropic D4d Spin Qubits as Nodes of a Gd(III)-Based Metal-Organic Framework. *Inorganic Chemistry*, 8575-8580.

J. Sumarkeris, J. J. (2005). Bulk crystal growth, epitaxy and defect reduction in silicon carbide materials for microwave and power devices. *MRS Bulletin, 30*(4), 280-386. Retrieved from 10.1557/mrs2005.74

K. Watanabe, K. Y. (1994). Kinetic inductance of superconducting coplanar waveguides. *Japanese Journal of Applied Physics, 33*(10R), 5708. doi:10.1143/JJAP.33.5708

L. Kuebler, E. H. (2024). The role of carbon capping and Ar pressure on SiC surface degradation during high temperature annealing. *Applied Surface Science*, 160654.

M. Göppl, A. F. (2008). Coplanar waveguide resonators for circuit quantum electrodynamics. *104*(113904). doi:10.1063/1.3010859

M. S. Khalil, M. J. (2012). An analysis for symmetric resonator transmission applied to superconducting devices. *Journal of Applied Physics, 111*(054510). doi:10.1063/1.3692073

Majumdar, R. D. (2015). *A nuclear meagnetic resonance spectroscopic investigation of the molecular structure and aggregation behaviour of asphaltenes.* Lethbridge, Alberta, Canada: Department of Chemistry and Biochemistry, University of Lethbridge.

N. T. Son, P. C. (2006). Divacancy in 4H-SiC. *Physical Review Letters, 96*(069902).

O. Suchoi, B. A. (2010). Intermode dephasing in a superconducting stripline resonator. *Physical Review B, 81*(174525). doi:10.1103/PhysRevB.81.174525

Palacios-Laloy, A. (2010). *Superconducting qubit in a resonator: test of the Legget-Garg inequilatiy and single-shot readout.* Universitie Pierre et Marie Curie, Paris. Retrieved from https://tel.archives-ouvertes.fr/tel-00815078

Pieter Kok, W. J. (2007). Linear optical quantum computing with photonic qubits. *Review of Modern Physics*, 135-174.

R. Igreja, C. J. (2004). Analytical evaluation of the interdigital electrodes capacitance for a multi-layered structure. *Sensors and Actuators A, 112*(291-301), 291-301.

S. A. Tarasenko, A. V. (2018). Spin and optical properties of silicon vacancies in silicon carbide - A review. *Physica Status Solidi B, 255*(1), 1700258.

S. Frasca, I. A. (2023). NBN films with high kinetic inductance for high-quality compact superconducting reonators. *Physical Review Applied*, 044021.

S. Probst, F. S. (2015). Efficient and robust analysis of complex scattering data under noise in microwave resonators. *Review of Scientific Instruments, 86*(024706). doi:10.1063/1.4907935

T. Ohshima, T. S. (2018). Creation of silicon carbide by proton beam writing toward quantum sensing applications. *Journal of Physics D:Applied Physics, 51*(33). doi:10.1088/1361-6463/aad0ec

T. Suzuki, T. Y. (1995). Neutron irradiation damage of silicon carbide. *Fusion Technology, 27*(3), 314-325. doi:10.13182/FST95-A30393

V. Ranjan, G. D. (2013). Probing dynamics of an electron spin-ensemble via a superconducting resonator. *Physical Review Letters, 110*(067004). doi:10.1103/PhysRevLett.110.67004

W. Hsu, S. L. (1999). In situ localized annealing for contamination resistance and enhanced stability in nickel micromechanical resonators. *12th International IEEE Micro Electro Mechanical Systems Conference* (pp. 453-458). Orlando: Technical Digest.

Xiaobo Zhu, S. S.-i. (2011). Coherent coupling of a superconducting flux qubit to an electron spin ensemble in diamond. *Nature*, 221-224.

Y. Kubo, F. R. (2010). Strong coupling of a spin ensemble to a superconducting resonator. *105*(140502), 140502.